Ocean Engineering 285 (2023) 115417

Contents lists available at ScienceDirect

Ocean Engineering

journal homepage: www.elsevier.com/locate/oceaneng

Variable buoyancy anchor deployment analysis for floating wind applications using a Marine Simulator

Rodrigo Martinez [a], Sergi Arnau [a], Callum Scullion [b], Paddy Collins [b], Richard D. Neilson [a], Marcin Kapitaniak [a,*]

[a] The National Decommissioning Centre, School of Engineering, University of Aberdeen, Newburgh, AB41 6AA, UK
[b] Aubin Group, Castle Street, Castlepark Industrial Estate, Ellon, AB41 9RF, UK

ARTICLE INFO

Keywords:
Marine simulator
Virtual prototyping
Underwater towing operation
Anchor dynamics
Floating wind

ABSTRACT

To study the feasibility of deploying a novel type of anchor with variable buoyancy for mooring floating offshore wind turbines, a set of detailed modelling studies was performed in the state of-the-art Marine Simulator at the National Decommissioning Centre. The aim of the multiphysics simulations is to assess fully a proposed craneless deployment method that involves towing the anchor from the harbour to the installation site, pumping liquid ballast to overcome anchor's buoyancy and lowering it to the seabed using only a winch, thereby simplifying the process, and reducing installation costs. As a test case, a novel shape of the floating anchor is considered, to establish the feasibility of its deployment in conjunction with the variable buoyancy technology and installation sequence. The analysis is divided into three sections: characterisation of the anchor buoyancy, positioning the anchor under the stern of the vessel and the controlled descent of the anchor to the seabed, under varying weather and operational conditions (e.g significant wave height, current, winch velocity, liquid ballast mass, ballast pump rate). The analysis allows assessment of the importance of the different factors affecting the proposed deployment scenario of variable buoyancy anchors, such as the winch velocity, the ballast mass and the pump rate.

1. Introduction

The economic drivers for lowering the Capital Expenditures (CapEx) and Operational Expenditures (OpEx) of Floating Offshore Wind Turbine (FOWT) technologies calls for innovation. In 2021, offshore wind capacity in Europe was predicted to increase to 27.9 GW by 2026 (WindEurope, 2022). This is an average of 5.6 GW per year. The UK is currently the European country with the largest offshore installed capacity, and it is predicted that its share of offshore wind will be 39% of the whole of Europe by 2026 (WindEurope, 2022). The Levelised Cost Of Electricity (LCOE) for FOWT between 50 and 100 m depths is currently comparable to fixed offshore wind turbines (Myhr et al., 2014).

Offshore wind turbines can be divided into two categories: floating (FOWT) and structures fixed to the seabed. Much of the offshore wind energy resource worldwide is located in deep water and current fixed-bottom turbine technology may not be an economical solution for developing these sites. However, floating offshore wind turbines allow this resource to be harnessed (Stewart and Muskulus, 2016a). Floating wind substructures are classified into four predominant types: semi-submersible, Tension Leg Platform (TLP), spar, and barge platforms. All of these require anchors for mooring to the seabed. Regardless of the anchor type, its deployment is usually done using established anchoring technologies/methodologies borrowed from the Oil & Gas industry (Bjerkseter and Agotnes, 2013). Extensive studies have been conducted on FOWT aerodynamics (Micallef and Rezaeiha, 2021; Stewart and Muskulus, 2016b) and their mooring systems (Liu et al., 2016). Academic research in this field is therefore essential to further understand the anchoring and mooring technologies specific to FOWT needs, in order to reduce their costs and ease of installation (James et al., 2018; Spearman et al., 2020). However, no extensive literature has been found on the design and development of novel anchoring technologies despite their potential for improvement (James and Ros, 2015; Strivens et al., 2021). In recent years, The Carbon Trust has developed a series of reports through the Floating Wind Joint Industry Project to try and develop further the maturity of FOWT (James et al., 2018; Spearman et al., 2020; Strivens et al., 2021; Harvey et al., 2022). Currently, information provided to developers by foundation suppliers is limited (Harvey et al., 2022). The published standard on floating wind turbine structures (Det Norske Veritas, 2018) along with

* Corresponding author.
E-mail address: Marcin.Kapitaniak@abdn.ac.uk (M. Kapitaniak).

https://doi.org/10.1016/j.oceaneng.2023.115417
Received 23 December 2022; Received in revised form 9 July 2023; Accepted 16 July 2023
Available online 25 July 2023

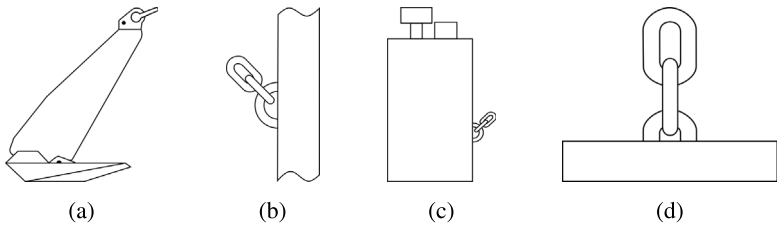

Fig. 1. Anchor types generally used in floating offshore wind.turbines: (a) drag-embedded, (b) driven pile, (c) suction pile, (d) gravity anchor.
Source: Adopted from James and Ros (2015).

knowledge obtained from it on support structures for bottom-fixed wind turbines (Det Norske Veritas, 2016), includes only a section on the design of anchor foundations. These documents outline the overall process and criteria required for designing anchors for FOWT.

Little information is found related to the particular type of anchors employed in different floating wind projects currently under development. However, knowledge from the Oil & Gas industry is adapted to meet the offshore wind requirements (James and Ros, 2015; Ikhennicheu et al., 2020; Brown, 2005; Ma et al., 2019). Fig. 1 shows the most common anchor types, which include drag-embedded, driven pile, suction pile and gravity based anchors currently used for floating wind applications (James and Ros, 2015). Each type of anchor has its own deployment procedure. Drag-embedded (a) and gravity (d) anchors are simply lowered to the seabed during their commissioning, whereas driven (b) and suction (c) piles need further interventions to complete their installation. The selection criteria for anchors is highly dependent on the seabed conditions at the particular deployment location. Hence, bathymetry and geotechnical surveys should be conducted as part of the planning process. In comparison with other types of anchors, gravity ones require medium to hard soils. Their main loading direction is vertical but can perform at different angles (Stevens and Rahim, 2014). A drawback of gravity anchors is their weight required to ensure they work efficiently. Consequently, this heavy mass increases installation costs as larger, less available and more costly heavy lift vessels are required. Moreover, this decreases the potential to recover the anchors upon decommissioning in the future.

The deployment of anchors and other offshore assets is limited by weather windows. These are characterised by a series of environmental conditions that allow for safe deployment of equipment (Walker et al., 2013; O'Connor et al., 2013). The main characteristics associated with those weather windows are the significant wave height H_S and flow velocity U. Average flow around the North Sea is usually below 1 m/s (~2 kn) (Vindenes et al., 2018; Davies and Furnes, 1980). However, in certain areas characterised by channels, straits or some other land features, this can reach up to 4 m/s (~8 kn) (Sellar and Wakelam, 2018; Sutherland et al., 2013). The North Sea is characterised by sea states of class I (MET Office, 2010) with an occurrence of over 60%, followed by class III sea states with an average occurrence of 20% (Boukhanovsky et al., 2007).

The challenges related to the installation of floating wind anchors listed above, especially the gravity based ones, call for innovation and the development of novel techniques that will address or at least minimise them. This is particularly important in view of the increased demand for floating wind installations, the relatively short timescales for delivery of those projects and the limited access to heavy lift vessels capable of handling high weight anchors. Moreover, if the new techniques allow for expansion of installation weather windows, which pose currently a significant limitation depending on the location, the whole process of installing floating wind farm anchors could be greatly accelerated and delivered in a more cost effective way. One of the solutions to those problems is to use variable buoyancy technology and floating anchors for future floating wind applications.

In this study, the feasibility of deploying a novel type of anchor with variable buoyancy currently under development by Aubin Group and Oceanetics for mooring FOWT is presented. A set of detailed modelling studies are performed using the state-of-the-art, real time, Marine Simulator at the National Decommissioning Centre (NDC), developed and supplied by the Offshore Simulator Centre AS (OSC) (Offshore Simulator Center AS, 2020). Using the multi-physics simulation suite allows for a more economical proof-of-concept approach, that will allow full assessment of the proposed deployment method and de-risk its future offshore installation. A few academic studies have already been published using OSC's simulation software, mainly focused on the improvement of the simulator by adding different types of sensors (Li et al., 2017; Sanfilippo, 2016, 2017) and control algorithms (Sanfilippo et al., 2016). However, there is a limited amount of literature focused on the development and validation of novel technologies (Xu et al., 2020) and operations (Yuan et al., 2020). Cheng et al. (2019b) and Cheng et al. (2019a) analysed a dynamic positioning (DP) model of a vessel under environmental conditions with a sensitivity analysis. Lastly, another study looked into human behaviour and training during anchor handling operations (Håvold et al., 2015).

By using the proposed floating anchor, the use of heavy-lifting cranes and large vessels could potentially be avoided, thereby reducing complexity and associated expenses. Instead, the anchor can be deployed from a smaller vessel, equipped with a simple winch. Once the anchor is towed to the deployment site, it is pumped with a liquid ballast and lowered to the seabed using a winch. The proposed anchor (Fig. 2) has the shape of a truncated pyramid with a 10 m square base and is 4.46 m high (eyebolt inclusive). The shape developed by Oceanetics allows for multiple mooring lines connection points, hence the anchor has 4 sides allowing for improved flexibility during installation. Although, the main holding capacity comes from the gravity of the anchor itself (once fully ballasted), when a horizontal load is applied to it, the anchor due to its shape will wedge itself into the sand seabed, delivering in turn improved embedding capabilities. This principle will apply also for anchors with different numbers of sides as long as the wedge shape is maintained. Moreover, there is a potential to utilise such system to share anchors between multiple floating wind turbines which ultimately can reduce installation costs and complexity (Pillai et al., 2022). The empty anchor used as a case study in this paper has an air mass of 163 tonnes. Once installed and full of liquid ballast (specific gravity SG $\approx$ 3) the anchor will have mass of 500 tonnes and provide the equivalent of a concrete gravity based anchor of the same mass.

Design with decommissioning in mind has been one of the main drivers for developing and studying in detail the new types of anchors, such as the one presented in this paper. Offshore decommissioning has shown a significant potential for cost savings if "design for decommissioning" is incorporated from the very beginning (Stokes, 2014). By making the future decommissioning the exact reverse of the installation process a huge cost saving can be achieved by optimising installation of anchors and mooring systems, as suggested by Ikhennicheu et al. (2020). The main cost reduction will come from utilising smaller vessels during installation/decommissioning (reduced number of vessel crew), not being so dependent on weather conditions (expanded weather

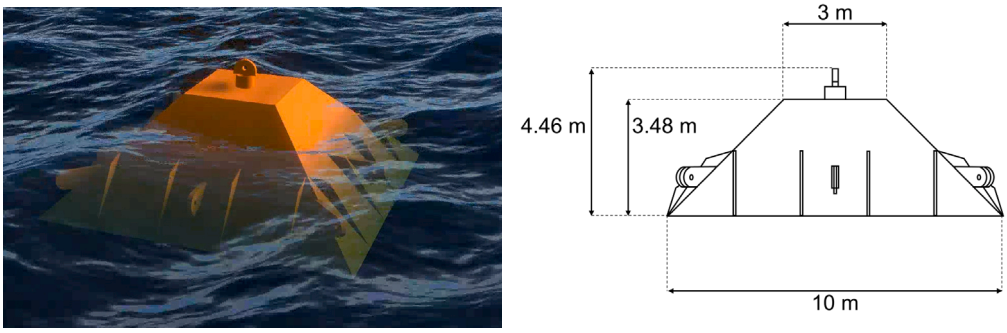

Fig. 2. Left: 3D representation of the anchor in the simulator's environment. Right: 2D diagram of the anchor.

window and reduced idle time), wider selection of available vessels, and not being limited by deck space (reduced number of trips to port). The four types of anchors described in Fig. 1 all require a specialised vessel and crew to complete installation, which in periods of higher demand can lead to an increase of the overall installation cost. The variable buoyancy anchor system presented here, on the contrary can float and be towed (including multiple anchors in arrays) from harbour to the deployment location. Utilising a smaller construction or anchor handling vessel should deliver further benefit in terms CO_2 savings, so vital in the quest for decarbonising offshore operations (ORE Catapult, 2021; Davies and Hastings, 2023).

The layout of this work is as follows. Section 2 goes over the concept of virtual prototyping, including a description of the Marine Simulator available at the NDC and a brief description of how the anchor interacts with its environment. The methodology adopted for the simulations is presented in Section 3. Here, the CAD model, tests/scene set-up, the testing procedure and test matrix are discussed. The simulation results are discussed and analysed in Section 4. Finally, conclusions and observations coming from the work undertaken are given in Section 5.

2. Virtual prototyping using NDC's Marine Simulator

Virtual prototyping can be described as computer simulations of a physical product (Wang, 2003), or as simulations for the purpose of design and functionality analyses in the early stages of the product development process (Pratt, 1995). In the field of offshore operations, virtual prototyping is still in its infancy. Virtual prototyping can be used to plan and validate missions to de-risk activities that are complex, not frequently performed, that require specific processes, specialised and/or bespoke equipment, that are performed in particularly harsh and remote environments or where there is little margin for errors (Major et al., 2021). In this area, modelling of offshore cranes has been of particular interest in recent years (Chu et al., 2018; Bye et al., 2015).

The Marine Simulator (Fig. 3) used in this work is located at the NDC at the University of Aberdeen. It is a real-physics (using software AGX Dynamics Algoryx Simulation AB, 2019), real-time simulator, capable of recreating irregular waves, currents and winds to de-risk offshore operations. Moreover, it is a walk-in, 300-degree visual immersive environment comprised of 16 projectors, and 4 stations with the ability to assign control of any object/asset placed in the scene (ROVs, cranes, personnel, vessels). Besides its graphics and visualisation, it allows collection of data (e.g. position, forces, velocities, accelerations etc.) for further analysis.

The simulator is comprised of a main computer in which the software Fathom, developed by OSC, is responsible of running the simulations. The scenarios where all the assets (vessels, ROV's, cranes, etc.) are imported and constrained are built in the Sandbox software, also developed by OSC. It is in the Sandbox where any environmental conditions to be investigated are set and implemented. Fathom is in charge of reading the inputs from the control chairs, analysing the physics and sending back the video data through Sandbox to the projectors and other screens. A more detailed explanation of the Simulator processes can be found in Xu et al. (2020), Yuan et al. (2020) and Offshore Simulator Center AS (2020).

The Marine Simulator relies on a series of algorithms to calculate the effects of wind, waves and currents on the objects imported into the simulator scene. The algorithms are based on recommended practices for modelling and analysis of marine operations (Det Norske Veritas, 2011) and on environmental conditions with their associated loads (Det Norske Veritas, 2014). In the Algoryx software, the simulation object is discretised into a triangulated mesh to compute the associated forces (Sandberg, 2014) acting on the structure. The summary of main hydrodynamics theories implemented into the Marine Simulator is given below.

- JOWNSAP spectrum S_J,

$$S_J(\omega) = A_\gamma S_{PM}(\omega)\gamma^r, \tag{1}$$

gives an approximation of the distribution of wave energy among different wave frequencies and wave-lengths on the sea surface. In Eq. (1), a peak enhancement factor γ^r is added (1) as the wave spectrum is never fully developed through wave-wave interactions and $A_\gamma = 1 - 0.287\ln(\gamma)$ is a normalising factor, while

$$r = \exp\left[-\frac{(\omega-\omega_p)^2}{2\sigma^2\omega_p^2}\right] \quad \text{and} \quad \sigma = \begin{cases}\sigma_1 = 0.07, & \text{for } \omega \le \omega_p.\\ \sigma_2 = 0.09, & \text{for } \omega > \omega_p.\end{cases} \tag{2}$$

The JONSWAP spectrum was proposed by Hasselmann et al. (1973) and is a modified spectra version of the Pierson–Moskowitz Spectrum S_{PM} (Pierson Jr. and Moskowitz, 1964),

$$S_{PM}(\omega) = \frac{\alpha g^2}{\omega^5}\exp\left[-\frac{5}{4}\left(\frac{\omega_p}{\omega}\right)^4\right], \tag{3}$$

where g is the acceleration due to gravity, $\omega = 2\pi f$ (where f is the wave frequency [Hz]), $\alpha = 8.1\times10^{-3}$, $\omega_p = g/U_{19.5}$ and $U_{19.5}$ is the wind speed at a height above the sea surface.

- Influence of waves in the flow velocity extends down the water column. How deep this goes depends on the wave parameters. This impact in the flow velocity can be quantified with linear wave theory using the general approach for intermediate waters (see, for example, Hedges, 1987; Dean and Dalrymple, 1984). This theory helps estimate the horizontal particle velocity at a desired depth as:

$$u = \frac{H}{2}\cdot\frac{\cosh[k(d+z)]}{\sinh(kd)}\cdot\omega\cdot\cos(kx-\omega t), \tag{4}$$

Fig. 3. View of the 300 deg toroidal dome (9 m diameter) visualisation suite of the NDC Marine Simulator. The system consists of 22 pcs (8 to run 16 projectors, 8 to run 4 control chairs and 6 to run the physics engine of the software). Assignable chairs are shown in the picture, which can control 2 vessels and 2 cranes/ROVs at the same time, therefore allowing for simulating operational scenarios involving simultaneous operation of these assets.

where H is the wave height, ω is the wave frequency, k is the wave number, d is the water depth, z is the height in the water column, x is the distance travelled in the streamwise direction and t is the time elapsed. $z = 0$ at the sea water level (SWL) and is positive vertically upwards.To find the wave number $k = \frac{2\pi}{L}$, it is necessary to find the wavelength L as:

$$L = \frac{gTw^2}{2\pi} \tanh\left(\frac{2\pi d}{L}\right), \tag{5}$$

where T is the wave period.

- Waves superimposed on a mean current experience a Doppler shift, which is the change in frequency of a wave from the reference frame of an observer who is moving relative to the wave source. This change in frequency is defined as:

$$\sigma = \omega - kU, \tag{6}$$

where ω is the rotational frequency of waves seen from a reference frame in which U is the current velocity, σ is the rotational frequency of waves seen from a reference frame in which $U = 0$ (i.e. the viewer is moving with the current). Free propagating waves only exist when the angular frequency ω and wave number k satisfy the frequency dispersion relation. The dispersion relation for intermediate waters according to (e.g.) Peregrine (1976) is defined as:

$$\Omega = \sqrt{gk \tanh kd} \quad \text{and} \quad \Omega^2 = \sigma^2. \tag{7}$$

Combining Eqs. (6) and (7) gives a dispersion relation with Doppler shift:

$$\omega = kU \pm \sqrt{gk \tanh kd} \tag{8}$$

The Doppler shift from Eq. (8), the horizontal particle velocity from Eq. (4) and the current velocity U, provide inputs for Algoryx's AGX Hydrodynamics module, which in turn allows the software to compute at each time step the buoyancy F_b, lift F_l, pressure F_p and viscous drag F_v forces acting on the anchor (or any other object considered) as:

$$\mathrm{F}_b = -\iint p_s \, \hat{\mathrm{n}} \, \mathrm{d}S = -\rho g \iint h \, \hat{\mathrm{n}} \, \mathrm{d}S, \tag{9}$$

$$\mathrm{F}_p = -\iint \frac{1}{2}\rho \, C_p \, (\mathrm{v} \cdot \hat{\mathrm{n}})^2 \, \mathrm{sgn}\,(\mathrm{v} \cdot \hat{\mathrm{n}}) \, \hat{\mathrm{n}} \, \mathrm{d}S, \tag{10}$$

$$\mathrm{F}_l = -\iint \frac{1}{2}\rho \, C_l \, (\mathrm{v} \cdot \hat{\mathrm{t}}_v)^2 \, \hat{\mathrm{n}} \, \mathrm{d}S, \tag{11}$$

$$\mathrm{F}_v = -\iint \frac{1}{2}\rho \, C_v \, (\mathrm{v} \cdot \hat{\mathrm{t}}_v)^2 \, \hat{\mathrm{t}}_v \, \mathrm{d}S, \tag{12}$$

where v is the flow velocity at the anchor's surface, ρ is the density of the fluid, $\hat{\mathrm{n}}$ is a unit vector normal to the mesh triangle, $\hat{\mathrm{t}_v}$ is the direction of the velocity tangent to the surface and C_p, C_v and C_l are the pressure, viscous drag and lift coefficients, respectively.

3. Methodology

3.1. Model description and setup

The proposed 3D anchor (Fig. 2) CAD model is imported into the Sandbox software with the appropriate collision model. The schematic of the anchor is depicted in Fig. 4 (left). The anchor has a base width of 10.00 m, body height of 3.48 m, overall height of 4.46 m and mass in air of 163.20 t. The inertia properties of the steel anchor body are calculated based on the CAD drawing and are imported into the Simulator as part of the collision model. Collision model generation is based on creating a mesh structure to represent the anchor and is generated using the software 3DS Max before importing it into the Simulator. Due to the software only taking into account the volume of the steel plates and internal bulkheads used to create the anchor shape, it is necessary to create a solid part that will represent the inner volume of the anchor (Fig. 4 (right)). This inner volume is filled/emptied to modify the anchor's buoyancy. The inner volume is fixed to the anchor within the Simulator environment. The model of the anchor is then assembled with the two components depicted in Fig. 4, where the inner volume representing the air/liquid is fixed rigidly inside the anchor. In order to ensure that the anchor floats, the inner volume is assigned a mass of 170 kg, which corresponds to the inner volume of 142.44 m^3 filled with air. The anchor is connected to the hose reel, using a standard 4" hose and a 50 mm OD steel winch cable.

In Fig. 5 we depict the triangular mesh applied to the anchor considered in this study. The anchor itself (or any other object simulated) is considered as a rigid body, with 6 degrees-of-freedom around its centre of mass (corresponding to the origin of the rectangular coordinate

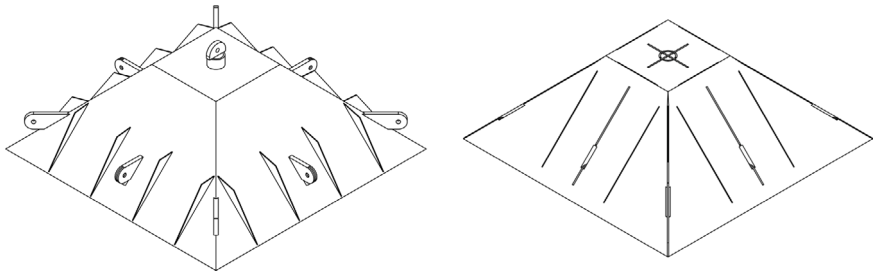

Fig. 4. Left: 3D model of the anchor. Right: 3D representation of the anchor's inner volume.

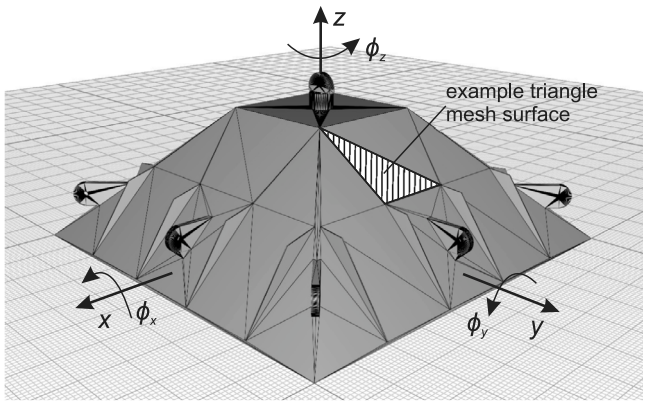

Fig. 5. Triangular mesh representation applied to the anchor model. The anchor is modelled as a rigid body with 6 degrees-of-freedom and environmental loading applied to individual mesh triangles.

system), while the overall environmental forces acting onto it are computed based on the forces acting onto the individual triangles.

A simple heave compensation system consisting of an axial spring of stiffness $k_z = 1000\ \frac{\text{kN}}{\text{m}}$ was added to the simulation between the winch cable and anchor's hook. A diagram of the system is shown enclosed in a green circle in Fig. 6, where the anchor deployment process is depicted. The developed scenario assumes that the floating anchor will be towed to the site and deployed from an anchor handling vessel equipped with a winch and a hose reel. As shown in Fig. 6.1, the floating anchor is connected to the winch using a cable and through a hose to the reel. Through the hose, the ballast fluid is pumped into the anchor. Once the anchor has negative buoyancy, it starts sinking and positions itself under the stern of the vessel, eventually hanging on the winch cable (Fig. 6.2). At this point, the anchor starts its controlled descent to the seabed guided by the winch at the desired velocity (Fig. 6.3). In this study, we use a specific anchor handling vessel, Buorbonic Arctic, available in the Marine Simulator library. However, the choice of vessel type will not have a significant direct influence on the detailed analysis of the deployment process presented in this paper.

The simulation scenario assumes that the anchor is deployed into 100 m water depth with ocean conditions represented by irregular waves using the JONSWAP spectrum with significant wave height of 1 m, current of 0.1 kn and peak period of 10 s. Note that both waves and currents are applied along the Y direction (as defined in Fig. 6), but the anchor itself has 6 degrees-of-freedom, which in turn allows the full 3D trajectories to be observed. Although the addition of wind is possible in the Marine Simulator, it was decided not to include this in the first round of tests as the anchor has a high draft when floating and its main interaction with the environment is limited to below the surface.

In order to illustrate what type of data can be collected from the Marine Simulator, we show below a few examples of time histories for the main parameters and the corresponding 3D trajectories of the anchor for both the positioning (2) and deployment (3) stages. The variation of the winch force F_W, anchor vertical position Z_A with the pump rate Q are shown in Fig. 7(a)–(b), where example time histories are presented for 3 sets of pumping rates (marked in blue, orange and yellow). Vertical dashed lines indicate the time at which F_W and Z_A stabilise. At faster pump rates ($Q \approx 1$ m^3/min), the anchor can be positioned underneath the stern of the vessel in just under 5 min. In contrast, at slower pump rates ($Q \approx 0.06$ m^3/min), the anchor takes up to 35 min to position itself below the vessel. Moreover, in the initial state the winch force remains constant as the anchor is still buoyant at this stage (before enough ballast gets pumped into it). Due to length of the cable, the forces acting on the winch cable F_W remain constant until the anchor is roughly 18 m under the water surface. The anchor 3D trajectories from the sea surface to underneath the vessel are shown in Fig. 7(c) and correspond to the cases depicted in panels (a)–(b). Note, that in this 3D plot the anchor starts initially at point (0,0,−3.2) [m], which corresponds to its starting position and ends at the final position beneath the stern of the vessel (−10,0,−18) [m]. At the lowest pump rate, the trajectory shows oscillations of the anchor due to wave motion. This is thought to be associated with the extended time it takes for the anchor to reach the position underneath the vessel's stern, making it more susceptible to wave-induced effects. In the same way, Fig. 7(d)–(f) depicts example time histories of F_W and Z_A and the corresponding 3D trajectories for 3 sets of winch velocities, (stage (3)), which illustrates the anchor's descent from beneath the vessel to the seabed (depth of 100 m). The trajectories shown in panel (f) indicate that the anchor's drift in the direction of waves increases as the winch velocity increases. Both the winch force and anchor vertical position increase linearly with time for a given winch velocity V_W. Note, that panel (d) depicts only the increase in force due to increased length of the winch cable (anchor weight in water is subtracted). The examples shown demonstrate the types of data that is collected from the developed model to study in detail in Section 4 the effects of the operational parameters and environmental conditions on the installation process (see Fig. 6).

4. Results

The analysis of the deployment process is divided into three sections: (1) characterisation of the anchor's buoyancy (see Section 4.1), (2) positioning of the anchor under the stern of the vessel by pumping ballast into it to create negative buoyancy (see Section 4.2) and, (3) controlled/guided descent of the anchor to the seabed by a winch (see Section 4.3.1). Subsequently in Sections 4.3.2 and 4.3.3 the effects of the significant wave height H_S and underwater current velocity v on the anchor descent phase are established.

4.1. Anchor buoyancy

To determine the buoyancy limit of the anchor when filled with air, its mass is increased until the anchor is fully submerged. This is

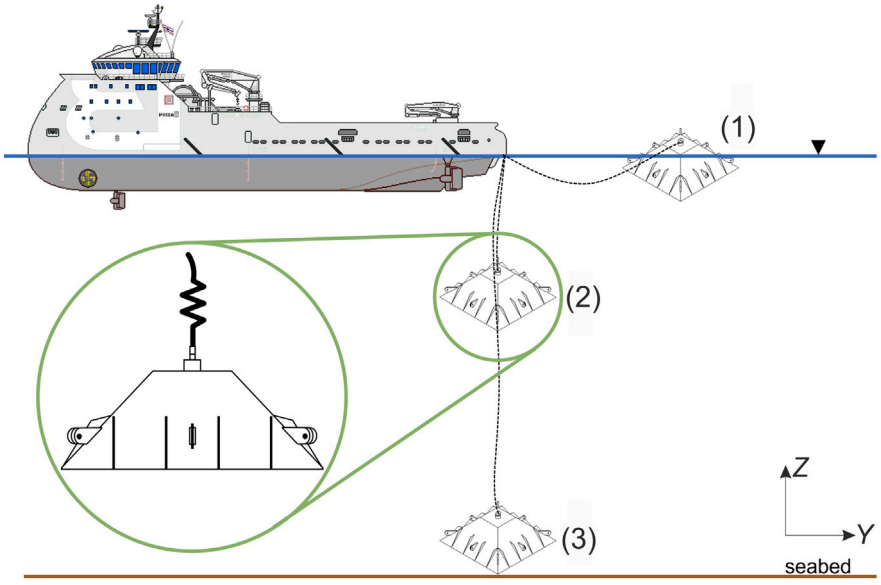

Fig. 6. Schematic of the deployment process of the anchor at deployment position: (1) initial position, pumping of ballast commences to generate negative buoyancy. (2) positioning of the anchor underneath the vessel's stern. (3) controlled descent of the anchor by means of a simple winch. A diagram of the heave compensation system used in the simulation is shown within the zoomed-in area in the green circle.

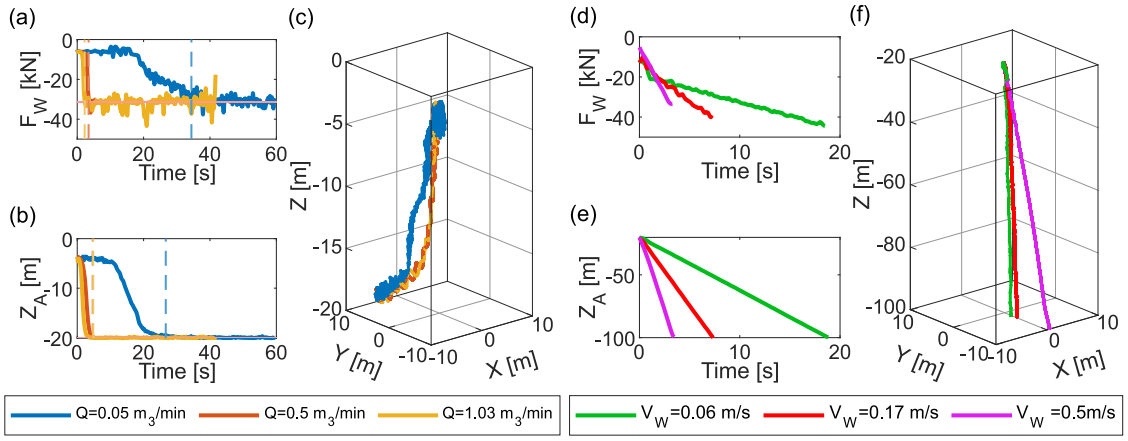

Fig. 7. Time histories for winch force (a,d) and anchor vertical position (b,e) for anchor positioning (a,b) and descent (d,e). Vertical dashed lines represent the time at which the signals stabilise. 3D trajectories for anchor positioning (c) and descent (f). Positioning sample tests are for Q = 0.05, 0.29 and 0.97 m^3/min. Descent sample tests for V_W = 0.06, 0.17 and 0.5 m/s.

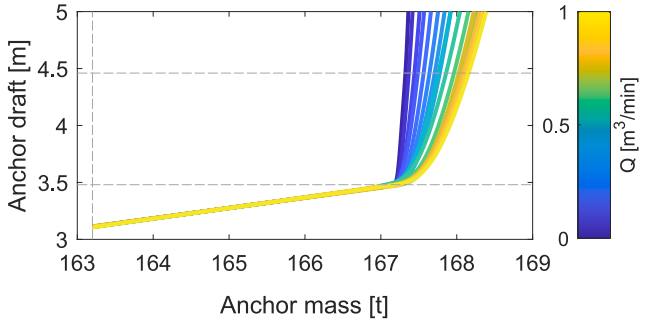

Fig. 8. Anchor buoyancy tests as a function of pump flow rate Q. Vertical line represents the weight of the anchor in air. The bottom horizontal line represent the height of the anchor without eye-bolt, the top line takes into consideration the height of the eye-bolt. Blue is for the slowest Q values. Yellow is for the fastest Q values.

achieved by increasing the rate, Q, at which the ballast is pumped into the anchor. Pump rates values from 0.04 to 1.87 m^3/min were used (see Table 1 for all Q values). The anchor buoyancy characterisation is shown in Fig. 8, where each curve corresponds to a specific pump rate. The vertical dashed line corresponds to the actual mass in air of the anchor (m_A = 163.2 t), while the two horizontal dashed lines denote the anchor body height (3.48 m) and overall anchor height (4.46 m), respectively. As shown, the buoyancy characteristics of the anchor change when its draft reaches the lower dashed line (167.3 t), which means that the anchor body is fully submerged and only the lifting hook remains above the water level. After this point there is a sharp change in the buoyancy characteristics and the precise point where anchor is fully submerged can be determined from the crossing point between the curve and the top horizontal line (lifting hook at the water level). This observed variation is directly related to how fast the ballast is pumped into the anchor. When the anchor mass reaches between 167 and 168 t, depending on the pump rate, the anchor becomes neutrally buoyant.

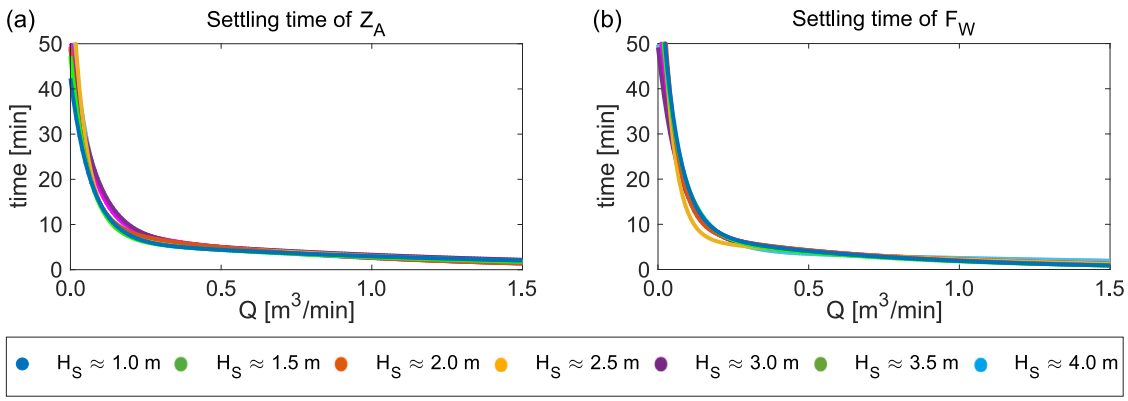

Fig. 9. Variation of anchor vertical position Z_A (red) and winch force F_W (blue) settling times with pump rate Q at different significant wave heights.

This means that the anchor possesses a gross buoyancy of about 4 t. The difference between the pump rates is attributed to the inertia created by the speed at which the ballast is being pumped. From a practical point of view, it is more important to know the approximate buoyancy limit of the anchor, rather than the precise amount of ballast required for a given pump rate. This is related to the fact that the anchor needs to have a negative buoyancy so that its installation can proceed as planned in the deployment scenario shown in Fig. 6. Nevertheless, the simulation shown above allows us to pinpoint exactly the buoyancy limit of the anchor and observe that it varies depending on how fast the ballast is pumped into the anchor.

4.2. Anchor positioning

In this section, we explore how the variable buoyancy anchor behaves during its positioning underneath the vessel's stern (stage (2) of the deployment scenario shown in Fig. 6) for varying pump rate Q (m^3/min) and environmental conditions (significant wave height H_S ranging from 1 to 5 m). For each wave height tested, a range of ballast pumping rates from 0.05 to 1.5 m^3/min is analysed. For all cases, a ballast of mass $m_B = 6.3$ t is added on top of anchor's air mass, $m_A = 163.2$ t, to ensure the anchor has negative buoyancy. In total, 174 simulations were performed (see Tables 2 and 3 for all Q values). Note, that these simulations are run in real time, so the computational time required to obtain results is matched to the time depicted in figures throughout this paper.

In Fig. 9(a)–(b) we depict a parametric plot illustrating the settling times of anchor's vertical position and the winch force as a function of pump rate Q for different values of H_S. The settling times correspond to vertical dashed lines defined in Fig. 7(a)–(b). As illustrated in Fig. 7(a)–(b), the settling times of the anchor's vertical position and winch force does not necessarily align with each other, particularly for slower pump rates ($Q < 0.2$ m$^{3/min}$). This is related to the fact that anchor can reach its position beneath the stern of the vessel before the prescribed amount of ballast is pumped into it. In general, the settling time for both vertical position and winch force relationship with pump rate follows an inverse function irrespective of the wave height considered (see Fig. 9(a)–(b)). For example, when $H_S = 1$ m and $Q = 0.15$ m^3/min, the anchor reaches its position under the stern in around 10.5 min and before the winch force stabilises. This means that once the anchor is in its destination position, the ballast gets pumped for further 2 min. At $Q = 0.4$ m^3/min, both F_W and Z_A settle in 4.8 min for $H_S = 1$ m. From this point onwards, as the pump rate increases, the settling times of the anchor's position remain longer than the settling times of the winch force. For example for $Q = 1$ m^3/min, F_W settles in 1.9 min and Z_A settles in 2.9 min.

The force excerpted on the winch during positioning of the anchor under the stern of the vessel is recorded on the 3D parametric plot in Fig. 10(a), where the dependence of the winch force amplitude on the pump rate Q and significant wave height H_S is shown. Similarly Fig. 10(b), depicts the amplitude defined as a difference between the min/max values of the anchor's vertical position Z_A during positioning. Note that on both panels in Fig. 10, the dashed lines denote the mean winch force and mean vertical position of the anchor, while the solid lines mark the maximum and minimum values of these quantities (obtained through detrending time histories like the ones shown in Fig. 7(a)–(b)). The mean value of the winch force F_W remains constant as Q varies, but we can observe its variation as H_S increases. Up to $H_S = 3.0$ m, the mean value of F_W remains at -31 kN, while it starts to decrease for higher values of H_S (~ -23 kN for $H_S = 4.0$ m and ~ -20 kN for $H_S = 5.0$ m). This is directly related to the increasing amplitude of the anchor's vertical position, which increases with the wave height, as shown in Fig. 10(b). This behaviour is expected, as the anchor is kept relatively close to the surface, where it is subjected to wave loading. The amplitude of the force F_W varies with pump rate Q, with the highest amplitudes observed for $Q = 1.0$ $\frac{\text{m}^3}{\text{min}}$, for most wave heights considered, as shown in Fig. 10(a). Similarly as for the mean winch force, the mean vertical position of the anchor increases (moves closer to the surface) when H_S increases. Up to $H_S = 3.0$ m, the anchor remains on average at a depth of $\sim$20 m, moving upwards to $\sim$19 m and $\sim$18.7 m for $H_S = 4.0$ m and $H_S = 5.0$ m, respectively.

The analysis presented allows for some conclusions to be drawn regarding the feasibility and important factors to be considered during anchor's positioning stage, that will inform future offshore deployment plans. The main observation tells us that it is better to pump liquid ballast into the anchor with faster rates, as this limits the exposure to wave loading. Moreover, the significant wave height seems to have a limited influence on the time it takes for both anchor's vertical position (driven by the cable length) and winch force (driven by the anchor's weight in water) to settle. On the other hand, the wave height has a more profound effect on the oscillation amplitude of anchor's vertical position, Z_A, which increases with increasing wave height. As a consequence, the amplitude of the winch force will also be affected by the significant wave height.

4.3. Anchor descent

4.3.1. Base case

In contrast to the positioning tests, the anchor's descent tests are analysed as a function of the winch velocity V_W. A base case with $H_S = 1$ m and winch velocities (V_W) ranging from 0.025 to 0.5 m/s is established (see Table 4 for all V_W values). Time histories of the anchor's vertical position are presented in Fig. 11(b), where it can be

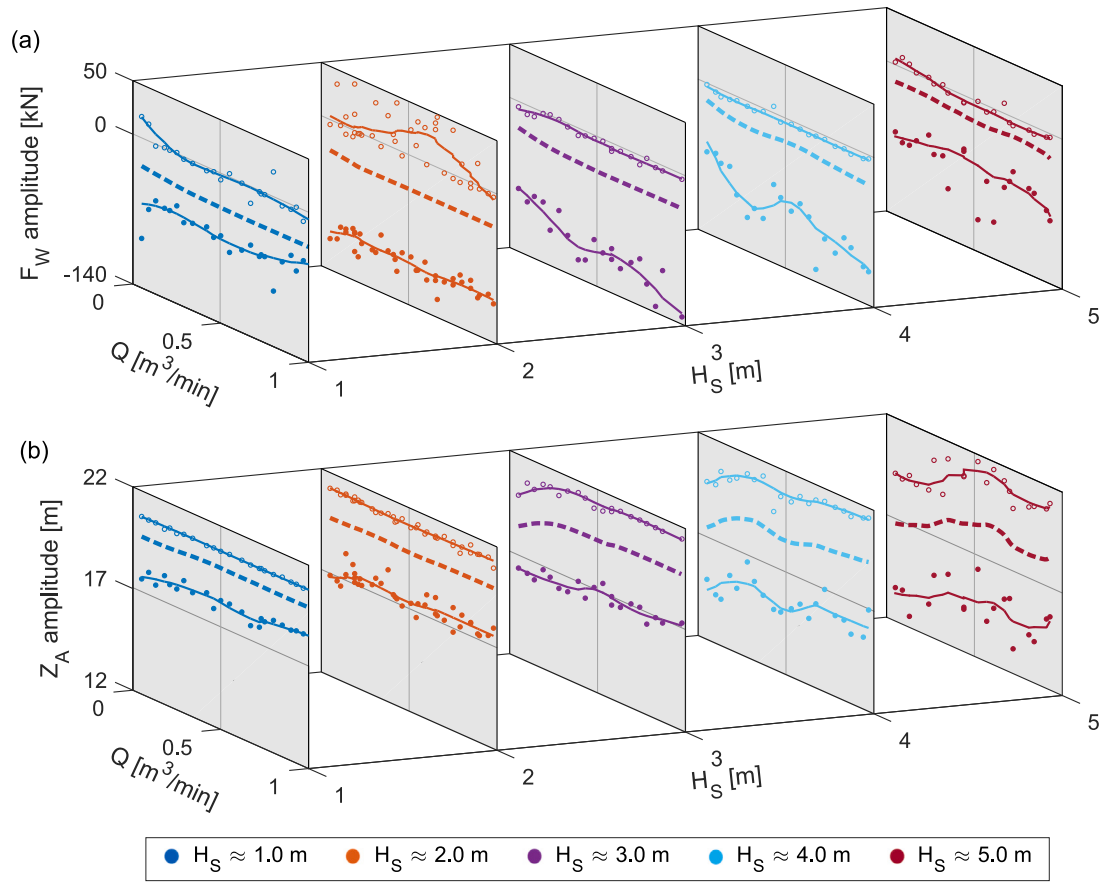

Fig. 10. Maximum (∘) and minimum (•) amplitude of the F_W (a) anchor's vertical position Z_A (b) for different wave heights. Each plane indicates a different H_S value. Dashed lines indicate the average winch force and vertical position of the anchor for a given significant wave height H_S and pump rate Q.

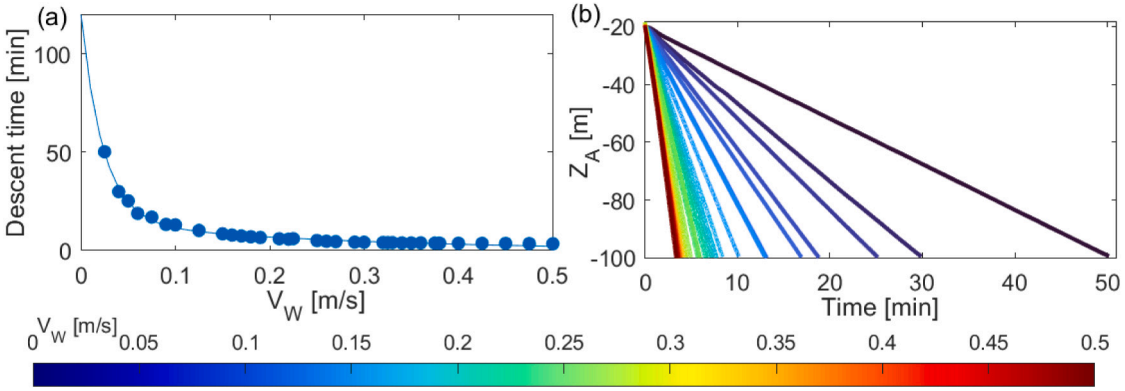

Fig. 11. Descent time from settling position to seabed as a function of winch velocity (a). Time histories of anchor's vertical position Z_A at all winch speeds V_W (b). Colour bar represents the winch velocity for each tests.

seen that the slowest it takes for the anchor to reach the seabed is 50 min (for the slowest winch velocity of 0.025 m/s). For the fastest winch velocities ($V_W > 0.5$ m/s), the anchor reaches the seabed in just over 3.5 min. Fig. 11(a) shows the time it takes for the anchor to reach the seafloor. Note, that the relationship describing the descent to seabed vs winch velocity follows a similar trend to that of positioning of the anchor under the vessel stern (see Fig. 9). It can be seen that for $V_W > 0.3$ m/s the descent time seems unchanged, whereas for $V_W < 0.3$ m/s the descent time increases considerably as V_W decreases.

First, let us explore the effect of waves on the anchor's vertical position and winch force as the anchor descends to the seabed. One factor that needs to be considered here relates to the interaction of the anchor and the vessel itself as it moves vertically due to wave loading. It is assumed that vessel motion is restricted to heave, pitch and roll degrees-of-freedom only as dynamic positioning is active. The winch cable connecting the anchor to the vessel, provides a coupling that can lead to some undesired behaviour. This is illustrated in Fig. 12, which depicts 3 example time histories for winch velocities 0.025,

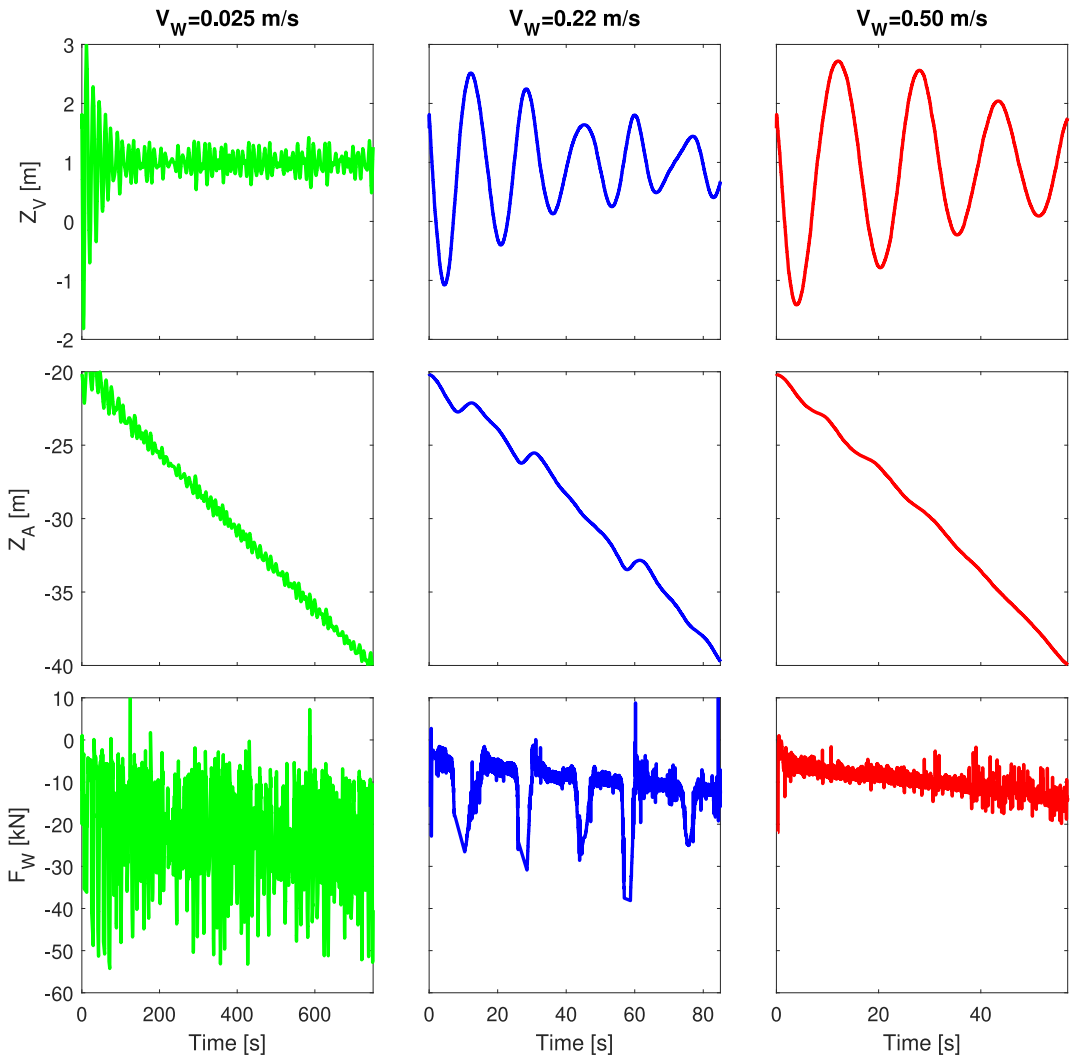

Fig. 12. Effect of waves on the anchor and winch forces: top - Vessel vertical position Z_V, middle - Anchor vertical position Z_A, bottom - Winch force F_W for three different winch velocities V_W (columns).

0.22, 0.50 m/s of the vessel's heave Z_V, the anchor's vertical position Z_A and the winch force F_W for a section of anchor's descent from depth of 20 m to 40 m. Note, that these graphs are restricted to showing examples in different time scales, as the focus is to compare the severity of the observed anchor vibrations in a given vertical section of the water column based on the chosen winch velocity. One can observe a clear coupling between Z_V and Z_A, which manifests itself in the slowed down descent of the anchor, with occasional upward movement of the anchor itself (best visible in the middle panel in Fig. 12) synchronised with an upward motion of the vessel. As the winch velocity V_W increases, the coupling between Z_V and Z_A becomes weaker as the winch cable is released faster than the anchor sinks, resulting in a smoother trajectory and much reduced number of spikes and lower average value of the winch force F_W, as shown in bottom panels in Fig. 12. The effect described above can be further eliminated (optimised) if a passive heave compensation system is used, which will require optimisation of the stiffness and damping characteristics of the connection point between the winch cable and the anchor itself. In our model this is represented by a simple spring/damper, while in real life commercial passive compensation systems based on the same principle can be used, if required.

From the analysis presented above, one can clearly see that the severity of coupling between the anchor's vertical position and vessel's heave motion diminishes with the winch velocity. In order to quantify that effect, an FFT analysis of a series of tests with multiple winch velocities is conducted and described below. Fig. 13(a) shows the isolated (detrended by subtracting the slope of Z_A shown in middle row panels of Fig. 12) oscillations of the anchor's vertical position Z_A for the three winch velocities shown in Fig. 12. At faster winch velocities, the oscillations have a smaller peak to peak amplitude (defined as the difference between min/max values) compared to the slower winch velocities. These oscillations decrease with time, as the anchor is further down the water column and the influence of the waves is reduced. The oscillations for the slower winch velocities have a pronounced frequency (Fig. 13(b)) at 0.07 Hz ($T = 14$ s) with a maximum peak to peak amplitude of 2.7 m. At higher winch velocities, the oscillations have a maximum amplitude of 0.5 m, more than 5 times smaller than that for the slowest winch speed. At $V_W = 0.22$ m/s, the observable oscillation frequencies have a range between 0.02 and 0.11 Hz ($T = 50$ and 9 s). In all cases we can clearly identify peaks, that correspond to the peak period $T_P = 10$ s, of the considered JONSWAP spectrum. The frequencies depicted in Fig. 13(b) allow one to visualise the effects observed earlier, that the severity of the anchor's vibrations diminishes as the winch velocity increases. Apart from the peak period of the spectrum, it is possible to identify other frequencies which are related to the stiffness of the winch cable. Moreover, they disappear as coupling of anchor's vertical position from the vessel's heave reduces with increasing winch velocity.

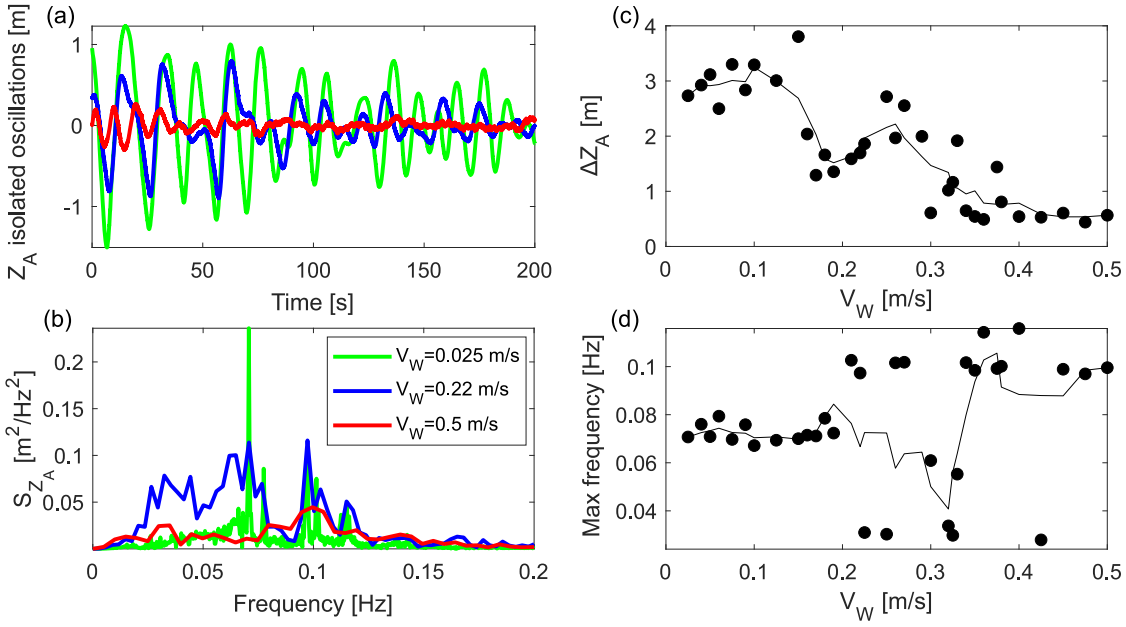

Fig. 13. Isolated oscillations of the anchor's vertical position (a) and anchor's vertical position in the frequency domain to identify main frequencies in the signal (b). Both panels for cases V_W = 0.025, 0.22 and 0.5 m/s. (c) The average amplitude of wave-induced oscillations in the anchor's vertical position and (d) maximum oscillation frequency of anchor's vertical position as a function of winch velocity.

Based on the analysis presented in Fig. 13(a)–(b), we can construct a parametric plot allowing the relationship between the peak to peak amplitude and the frequency of the oscillations induced by vessel's heave as a function of winch velocity to be observed, as shown in Fig. 13(c)–(d), respectively. The frequency at which the maximum amplitude of the oscillations is observed is shown in panel (d) (similar to Fig. 13(b)). For winch velocities below 0.2 m/s, the frequency remains constant at 0.7 Hz (T = 14 s). However, for winch velocities above 0.2 m/s and below 0.3 m/s, the maximum frequency of the oscillations is scattered with no visible trend. This is thought to be due to a small amplitude of the oscillations observed in the anchor's vertical position and the progressive decoupling of the anchor's vertical oscillations from the wave oscillations at the sea surface. As the winch velocity exceeds 0.3 m/s, a much clear trend is visible, with the maximum frequency of the observed oscillations reaching values close to the peak period of the wave spectrum. Panel (c) shows that the peak to peak amplitude of the oscillations decreases with increasing winch velocity. Above V_W = 0.15 m/s, we observe a significant drop in the observed amplitude, followed by a slight increase (local maximum at 0.25 m/s), and further consistent decrease of the amplitude with the winch velocity, until it eventually stabilises around an average value of 0.5 m at around $V_W > 0.35$ m/s. The parametric analysis presented above allows us to verify through FTT analysis and quantify the general trend, that the severity of the vessel's heave induced anchor oscillations diminishes as the winch velocity increases. This manifests itself in reduced peak to peak amplitude of anchor's vertical oscillations and the fact that dominant frequency observed in each time history is closely matched to the peak period of the JONSWAP spectrum applied.

Next, let us look into the anchor's X and Y positions at landing for all winch velocities V_W, as shown in Fig. 14. With no current present, it would be intuitive that for all winch speeds the landing position of the anchor would be very similar. This is correctly seen in the X position, where the anchor stays within ±1 m from its initial release position. The relatively small drift observed in the X direction originates from anchor's yaw, that gets induced during the positioning stage. As the anchor is unconstrained (apart from the winch cable) and has 6 degrees-of-freedom in the 3D simulation, there is a possibility for it to yaw during its positioning under the stern. Consequently, the anchor is no longer perpendicular to the wave direction, hence its drift in X can take place. On the other hand in the Y direction, there is a larger drift associated with the direction of wave propagation applied in the model (Y). This is an expected behaviour related to the well-known phenomenon of Stokes drift (Weber, 2021; Webb and Fox-Kemper, 2015; Henry, 2019). In this case, the anchor drifts up to 10 m from its release position. The 3D sinking trajectories are shown in Fig. 14(c). The trajectory is similar at all winch velocities. However, the faster the descent, the further the anchor drifts (up to 10 m) from its initial position in the Y direction (parallel to the wave propagation). This counter intuitive observation is further explored in the next paragraph.

Next, we investigate the relationship between anchor's descent velocity V_A and the winch velocity V_W, which is depicted in Fig. 15(a) for a significant wave height H_S = 1 m. The graph contains data for other wave heights as well, but these are discussed in detail in Section 4.3.2. It can be seen that for V_W values below 0.35 m/s the anchor descent is governed by the winch. However, at higher V_W values, the anchor reaches an equilibrium and its descent velocity should not increase (free fall marked by the vertical line), regardless of how fast the winch spools out the cable. Note that the slight increase in anchor's velocity above V_W = 0.37 m/s, visible in Fig. 15(a), is a consequence of an increased anchor weight due to loose cable connected to it. As the cable is winched out faster than the anchor sinks, the loose winch cable provides additional mass (≈62 kg per meter) that speeds up anchor's descent. The behaviour observed though this analysis is directly related to counter intuitive observations from Fig. 14, that indicate that anchor deviates more along Y direction for higher values of winch velocity. Namely, when the winch velocity is below the aforementioned threshold, the cable guides the anchor as it descends, even though as explained earlier more of the vessel's heave is passed towards the anchor. Above V_W = 0.35 m/s the guiding effect of the cable diminishes, hence the higher anchor's deviation in the Y direction, even though less of vessel's heave gets transferred to the anchor itself, due to decoupling. In practical terms, this can be further optimised. If our goal during installation is to limit anchor's deviation, then one can utilise appropriate passive heave compensator that will minimise the anchor's oscillations during its descent at lower values of winch velocity. In Fig. 15(b), the orientation range of the anchor is shown. The yaw range is the difference between the yaw angle at the time the anchor reaches the seabed and the angle from the moment the

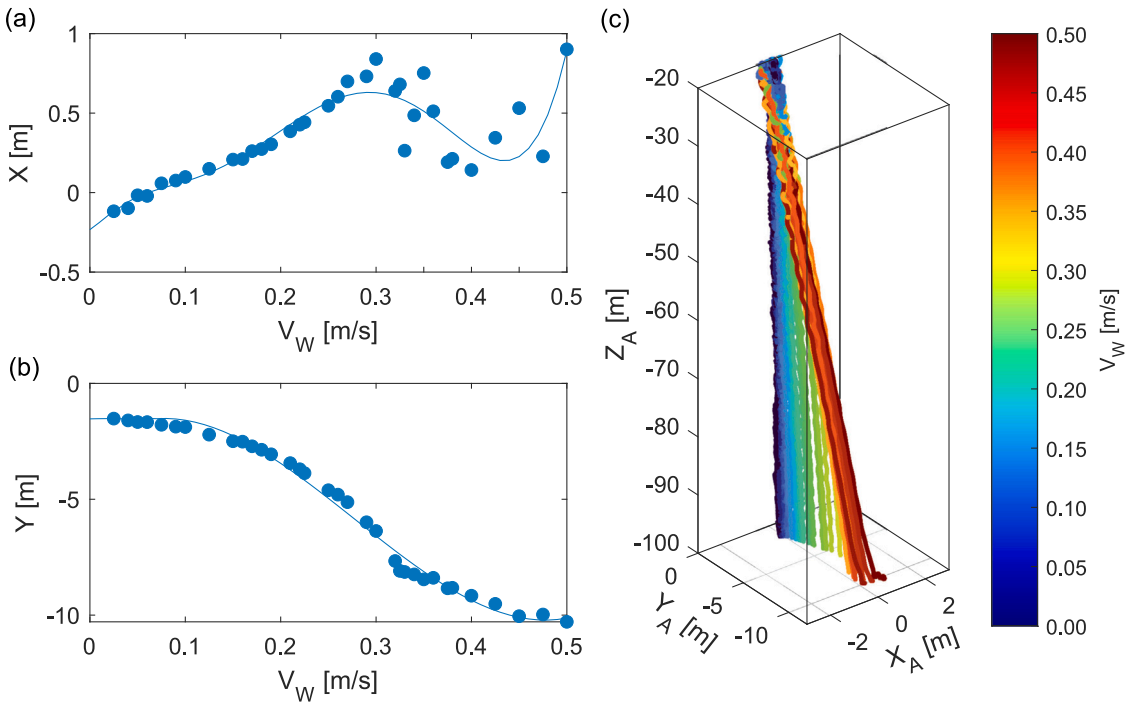

Fig. 14. Variation of the anchor drift in the X (a) and Y (b) directions for all winch velocities. Y axis is in the wave propagation direction. (c) 3D trajectories of the anchor's descent to the seabed from the settling position for all winch speeds V_W. Colour bar represents the winch velocity for each test.

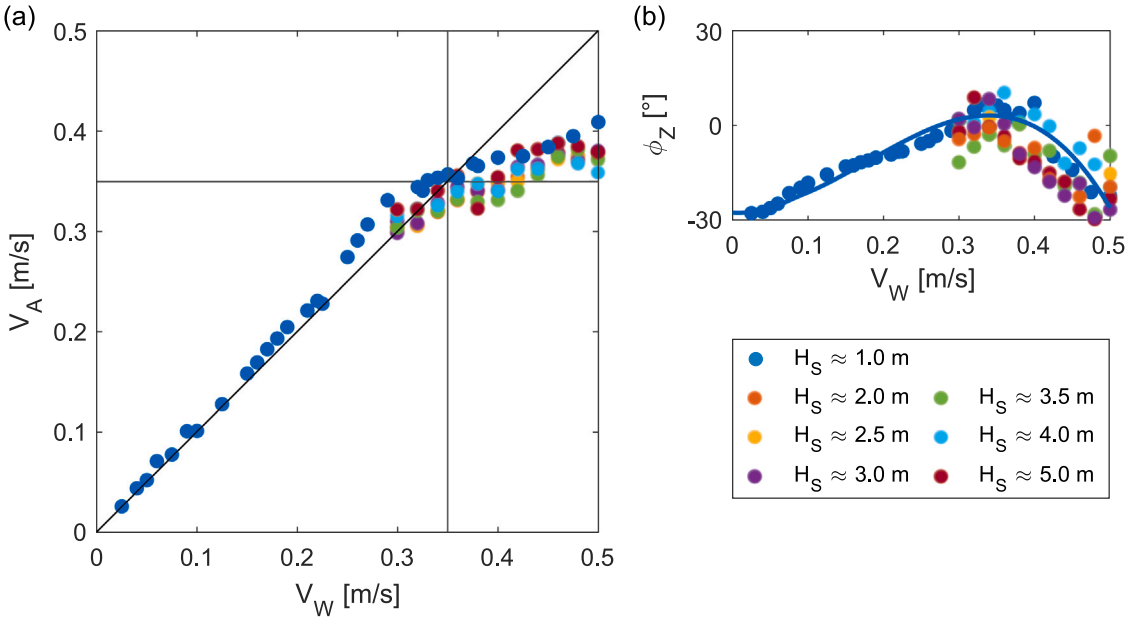

Fig. 15. (a) Variation of the anchor descent velocity (V_A) and (b) operational range of yaw (ϕ_Z) as a function of winch velocity (V_W) for wave heights $H_S \in (1, 5)$ m. The horizontal line marks anchor's free fall velocity in water, $V_A = 0.35$ m/s. The vertical line denotes the winch velocity equal to anchor's free fall velocity.

winch is released. The yaw angle ϕ_Z has a minimum value for winch velocities between 0.32 and 0.38 m/s, while outside that interval it increases significantly (up to 30 deg), which confirms further benefit of matching the winch velocity and free fall velocity of the anchor itself.

From the analysis presented above, we can make preliminary observations about the overall effects of the winch velocity on the anchor's descent. There is a clear trade-off, as using slower winch velocities results in a longer descent time and increased amplitude of oscillations related to vessel's heave (see Fig. 13(b)), while at the same time providing improved guidance of the anchor, due to lower deviations in the X and Y directions (see Fig. 14). On the other hand, as shown in Fig. 15, operating the winch above the free fall velocity of the anchor results in optimal conditions in terms of anchor's yaw, which in turn should prevent entanglement of the cables/hoses connected to the anchor. The subsequent analysis focuses on establishing the effect of significant wave height H_S on the anchor's descent in a narrower range of winch velocities between 0.3 and 0.5 m/s, as it allows optimal yaw response.

4.3.2. Effects of wave height

In this section, we study in detail the effect of significant wave height (interval: 2–5 m) on the variable buoyancy anchor's descent

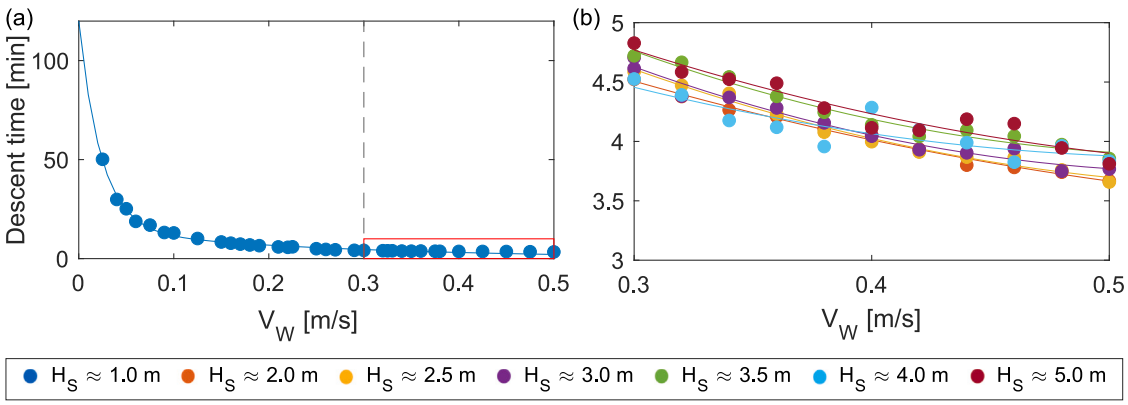

Fig. 16. Descent time as a function of winch velocity for all winch velocities. Base case with $H_S = 1$ m (a) and wave cases with H_S ranging from 2 to 5 m (b).

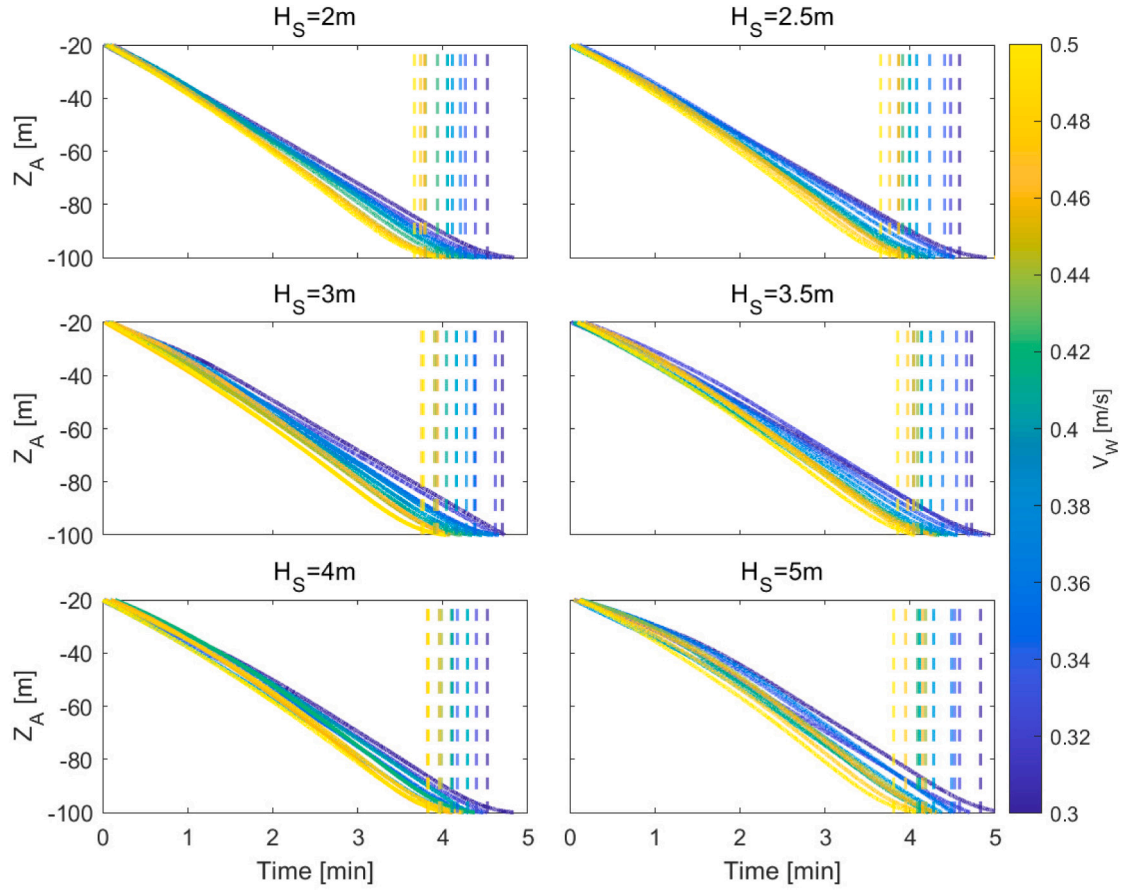

Fig. 17. Variation of the anchor's vertical position with time for all wave cases. Colour bar represents the winch velocity for all panels. Vertical dashed lines indicate the time at which the anchor reaches the seabed.

in a narrower window of winch velocities (0.3–0.5 m/s) identified as optimal and more beneficial from offshore deployment point of view (e.g. reduced descent time, reduced coupling to vessel's heave, minimum yaw angle during descent when winch velocity matches anchor's free fall velocity). A full set of tests carried out in this section and corresponding simulation parameters are presented in Table 5. Descent times for all wave heights are shown in Fig. 16(b), which depicts the considered interval marked by red a rectangle in panel (a) that shows the full set of results for the base case (see Section 4.3.1). Depending on the winch velocity (0.3–0.5 m/s), the anchor can be deployed within 4.7 and 3.7 min. Although there are small variations of the descent time when significant wave height changes, one can conclude that in general the H_S has no significant impact on the deployment time. On average, cases with $H_S = 5$ m, take roughly 0.3 min (18 s) longer that the cases with $H_S = 1$ m (Fig. 11(b)). Such time difference will have no significant impact on the whole installation process. For all considered wave heights the descent time follows the same trend as a function of winch velocity (inverse function observed earlier in Section 4.3.1). The small abrupt change for $H_S = 4$ m is attributed to a numerical error and is insignificant in terms of the general trend observed.

Next let us consider, how the significant wave height influences the vertical position of the anchor as it descends to the seabed. This is shown in Fig. 17, which is constructed in the same way as results presented earlier in Fig. 14(c). Each panel represents the data obtained for all winch velocities (0.3–0.5 m/s) for a specific wave height (see Table 5). The vertical lines mark the exact time the anchor reaches the

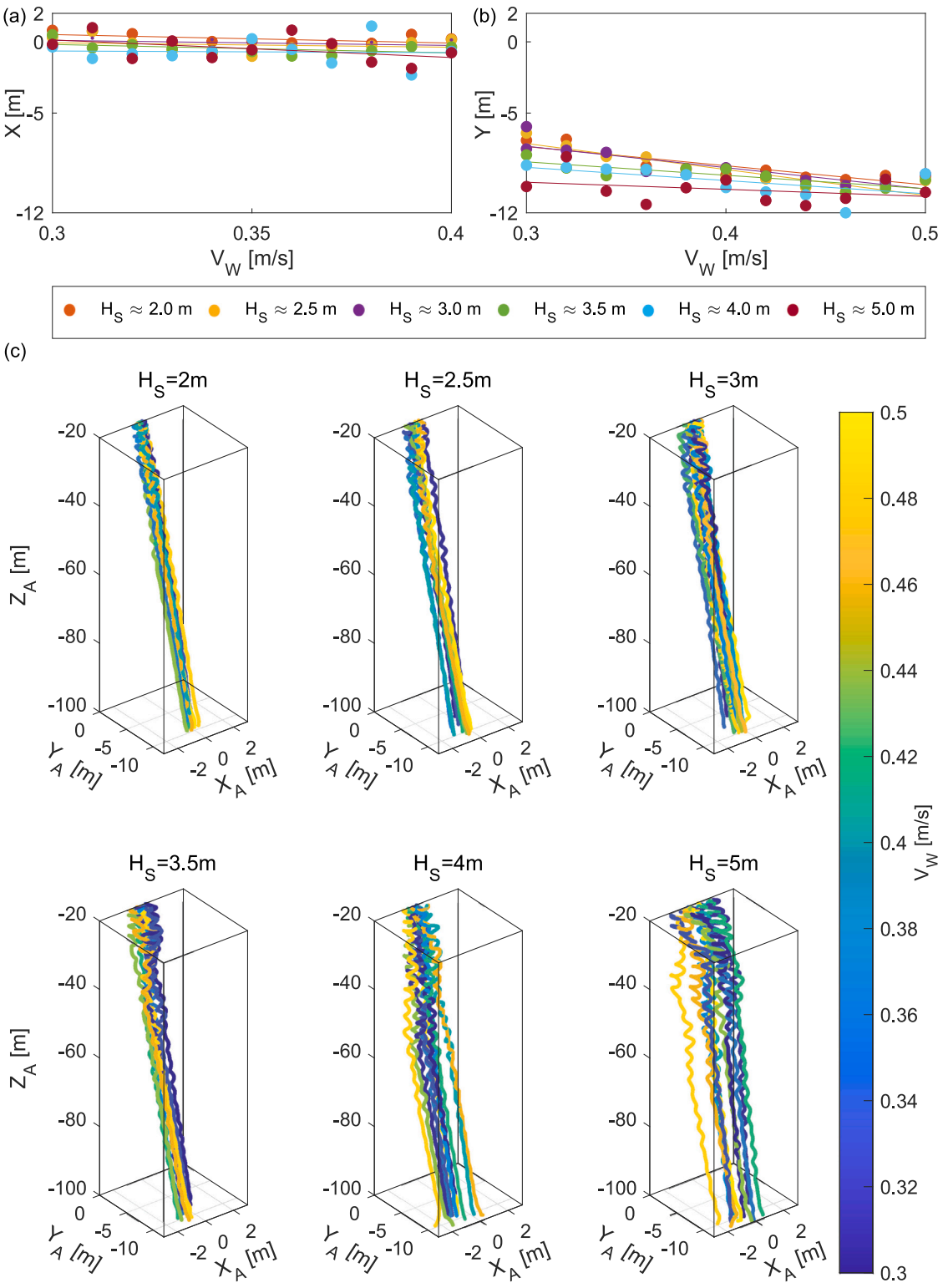

Fig. 18. Anchor landing position in the X (a) and Y (b) directions for all winch speeds and all wave heights. (c) 3D descent trajectories for all wave cases (2.0, 2.5, 3.0, 3.5, 4.0, 5.0 m) and winch velocities (0.3–0.5 m/s). Colour bar represents the winch velocity for all panels.

seabed. Comparing each of the panels, it is possible to see that, due to the heave compensation used in the winch, there are no significant wave-induced differences. However, it is thought that the anchor (due to its low weight in water) gets "trapped" closer to surface in higher waves, actively hindering its descent. This artefact can be seen in the descent time series, where there is a concave response at around $Z_A = -40$ m. Once, the anchor descends sufficiently low in the water column, its descent rate increases and is in line with lower wave height cases.

The drift of the anchor in the X and Y directions is explored in Fig. 18(a)–(b). It can be seen that the anchor lands further away in the Y direction by up to 12 m as wave height increases (red markers). In the X direction, however, the drift is minor, up to 2 m from the starting

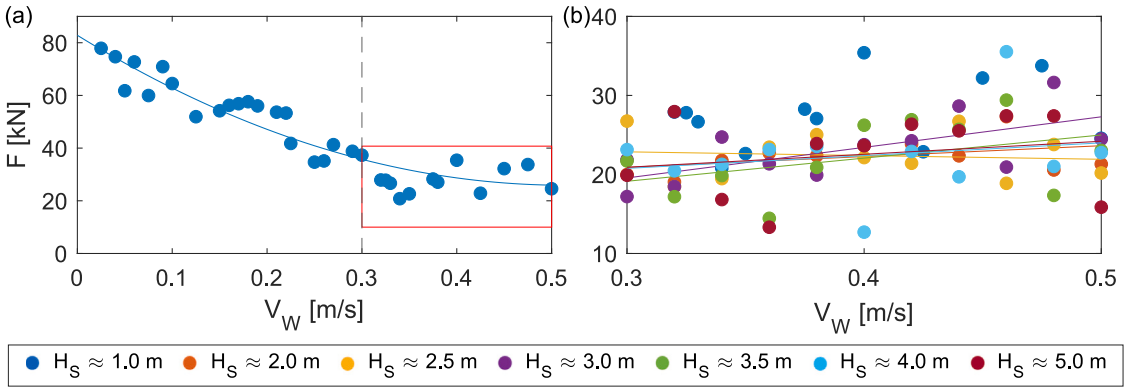

Fig. 19. Winch force range as a function of winch velocity. Base case with $H_S = 1$ m (a) and wave cases with H_S ranging from 2 to 5 m (b). Red rectangle on (a) refers to the axes limits on (b).

position. As explained in Section 4.3.1, the drift in X direction is related to the initial position and orientation of the anchor under vessel's stern. Fig. 18(c) shows the 3D trajectories of the anchor's descent for varying winch velocities and wave heights. As shown in Fig. 18(a)–(b), increasing drift along Y direction as wave height increases, is evident in the 3D trajectories. Interestingly, through the 3D trajectories we can observe the oscillations of the anchor on the X-Y plane as it descends to the seabed. Increasing significant wave height will increase the amplitude of the anchor's horizontal oscillations, particularly closer to surface. Nevertheless, these vibrations diminish as the anchor gets deeper in the water column, as shown in the 3D trajectories (Fig. 18). Vibrations observed on the way to the seabed have little impact on the overall landing position of the anchor itself, though from panel (b) one can see a correlation between wave height and increased drift in Y direction.

The orientation of the anchor for all of the above considered wave cases is superimposed onto the results for the base case (see Section 4.3.1) as shown in Fig. 15(a)–(b). The general behaviour of the anchor in terms of its descent velocity and induced yaw is very similar and follows the trends described already for the base case. Above $V_W = 0.35$ m/s the anchor's descent is decoupled from the winch, as the anchor moves slower than the winch. As for 1 m significant wave height case, the optimal value (minimum) of yaw occurs when winch velocity V_W is between 0.32 and 0.38 m/s. This indicates that overall effect of significant wave height on the variable anchor's orientation is minimal, and the main parameter that can induce yaw, possibly leading to cable entanglement issues, is the winch velocity. Hence, from the point of future offshore deployment plans this needs to be considered carefully.

Next, let us consider how the winch force changes with the winch velocity when the significant wave height varies. For a significant wave height $H_S = 1.0$ m, shown in Fig. 19(a), the results indicate that, in the presence of passive heave compensation, the working load peak to peak amplitude on the winch cable decreases from 80 kN at the lowest winch velocities to about 30 kN for $V_W > 0.35$ m/s. The spread visible in the force data is associated with the wave-induced oscillations. This observation can be linked to Fig. 15(a), where the winch has total control of the anchor's descent at $V_W < 0.35$ m/s, thus resulting in higher winch forces. Fig. 19(b) shows the force amplitude acting on the winch for all the wave cases ($H_S = 2$–5 m). This range is similar for all wave heights and does not present any trend associated with the winch speed. F_W has an average of 22 kN for $V_W < 0.35$ m/s, with maximum and minimum values of 32 and 12 kN, respectively. For $V_W > 0.35$ m/s we observe a higher degree of scattering of the winch force amplitude, which increases slightly with the winch velocity (scattering of the results makes it difficult to quantify precisely). This indicates further benefits of operating the winch at a velocity matched to the anchor's free fall velocity in water (dependent on the amount of ballast), as the observed force amplitude is reduced compared to lower winch velocities. The force variation can be further optimised during the installation phase by utilising passive heave compensation devices available within offshore industry. The increased drift of the anchor in the direction of waves for higher winch velocities can be addressed by either adjusting the vessel's position just before the anchor touches the seabed or by carefully estimating the appropriate initial position of the vessel based on site weather conditions and results presented in this paper.

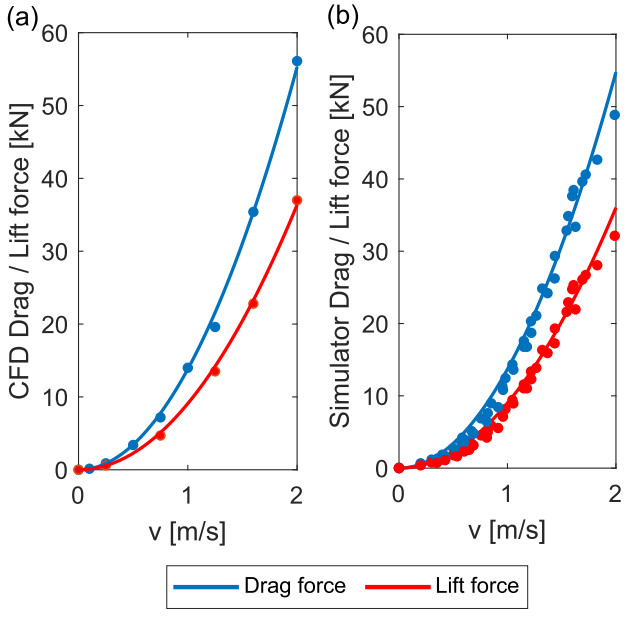

Fig. 20. (a) Drag and lift forces as a function of fluid velocity v from CFD analysis in ANSYS. (b) Calibrated response for drag and lift forces obtained from the Simulator. Lift and drag forces are marked in red and blue, respectively. The lift force acting on the anchor is negative, though only its magnitude is shown on the graphs.
Source: Adopted from Martinez et al. (2023a).

4.3.3. Effects of ocean currents

The effect that ocean currents have on anchor's descent is analysed in this Section. For that purpose, two variables are studied: four different ballast masses, (m_B: 6.3, 12.6, 25.2 and 31.5 tonnes) and current velocities ranging from 0 to 1 knots (see Table 6 for all values of m_B and U). Firstly, the local drag and lift coefficients used in the Simulator had to be calibrated. In order to achieve this, first a series of Computational Fluid Dynamics (CFD) simulations in ANSYS were conducted to establish the relationship between the drag/lift forces

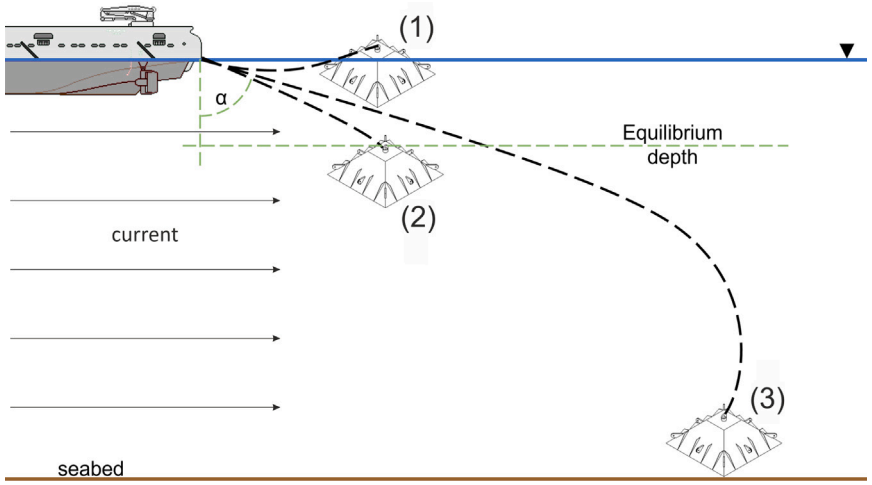

Fig. 21. Schematic showing the deployment process under influence of underwater current. (1) Ballast starts getting pumped into the anchor to create negative buoyancy. (2) Due to the currents, the anchor drifts in the current's direction while sinking until finds an equilibrium. (3) The anchor descends to the seabed and drifts in the current's direction, landing far from the initial deployment point.

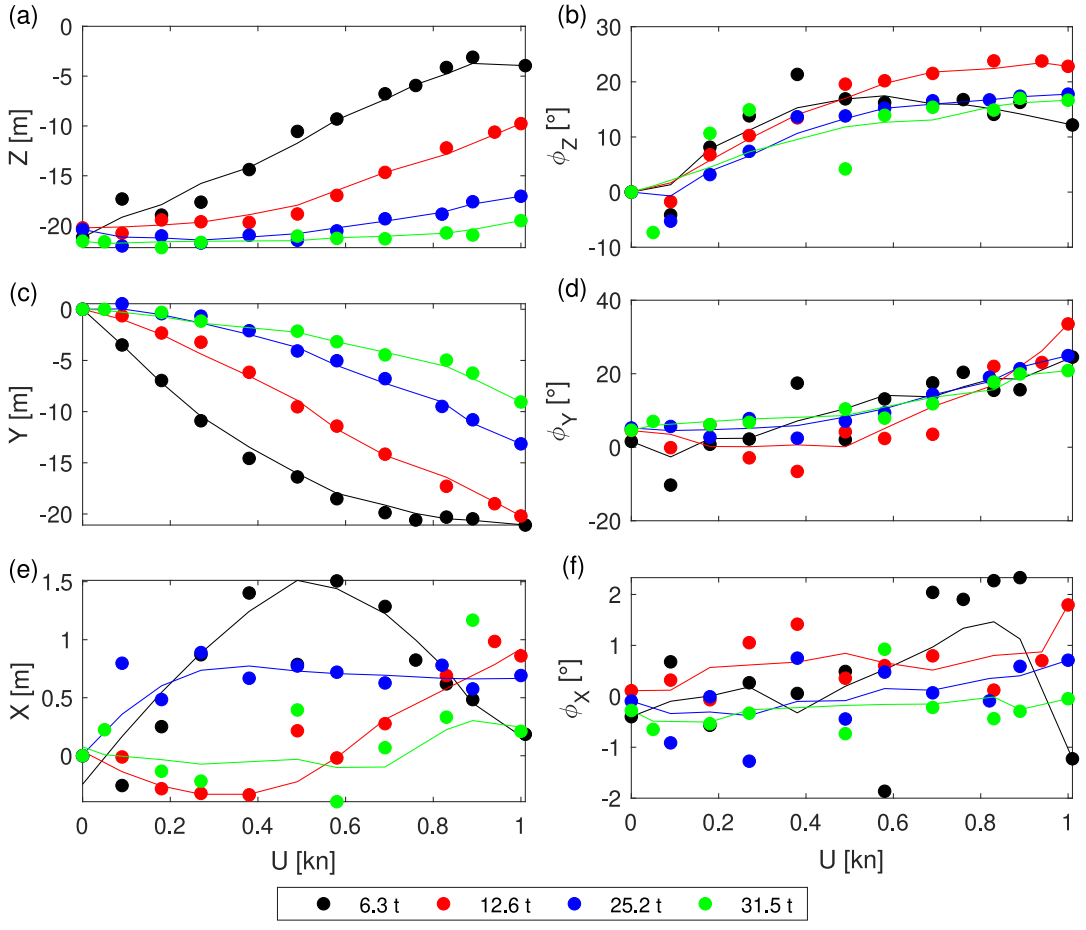

Fig. 22. Anchor's Z (a), Y (c) and X (e) position at the instant just before releasing the winch. Anchor's orientation yaw, ϕ_Z (b), pitch, ϕ_Y (d) and roll, ϕ_X (f) at the instant before releasing the winch. All panels are shown as a function of flow velocity U.

acting on the anchor as a function of fluid velocity v (See Martinez et al. (2023a) for more details regarding the CFD analysis and the calibration process). This is shown in Fig. 20(a), where the red and blue curves depict the lift and drag forces, respectively. Note, that the anchor has a negative lift force due to its shape, but the plot depicts its absolute value. Next, by identifying appropriate local drag/lift coefficients, the drag and lift force responses as a function of v were obtained, as shown in Fig. 20(b). Good agreement between the forces predicted through CFD and from the Simulator was achieved, which in turn allows us to study in detail the effects of ocean currents on the deployment

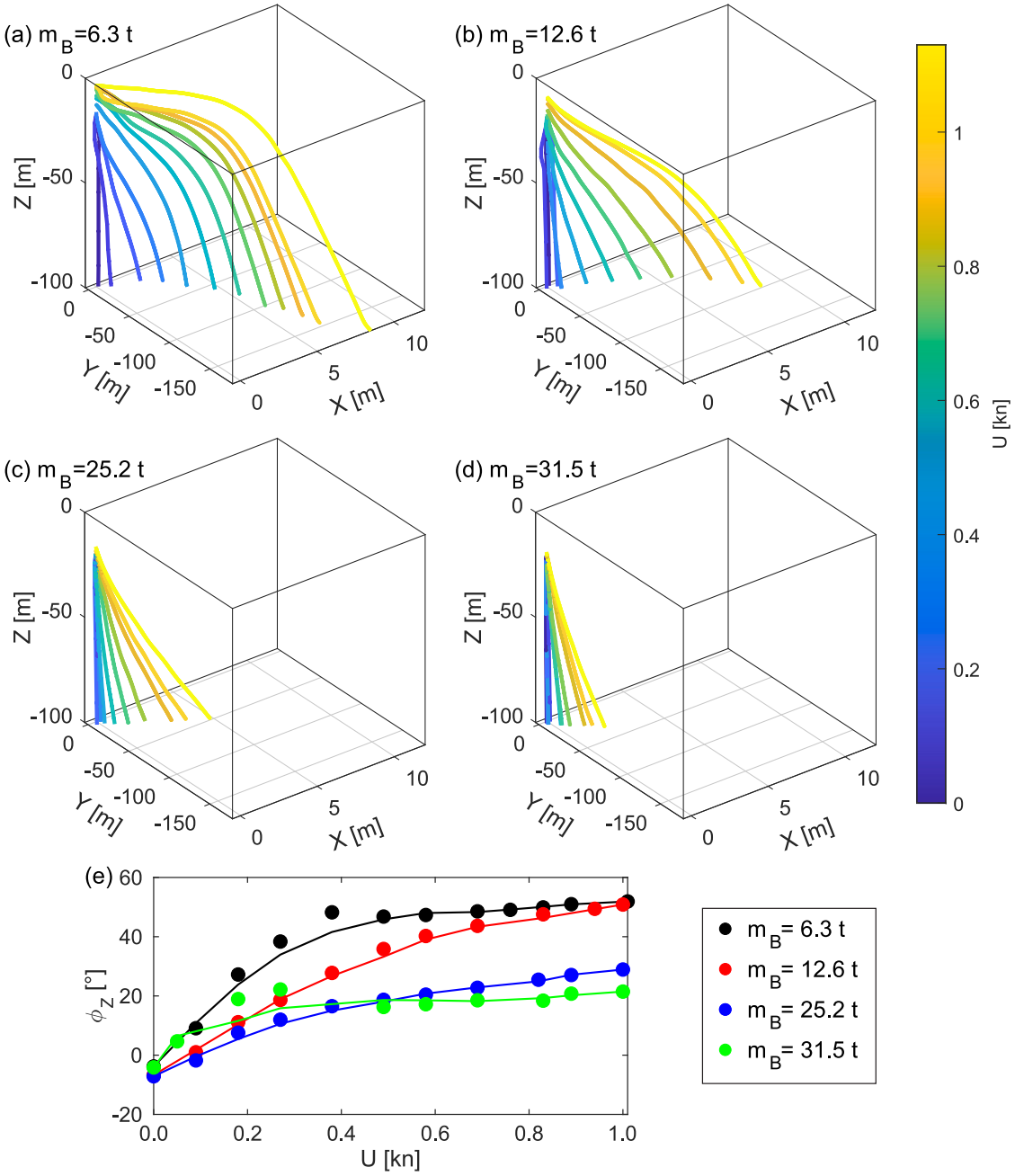

Fig. 23. 3D trajectories of anchor descent with a ballast mass of (a) $m_B = 6.3$ t, (b) $m_B = 12.6$ t, (c) $m_B = 25.2$ t and (d) $m_B = 31.5$ t for all flow velocities (0–1 kn). Colour of lines represent the flow velocity in knots. Anchor's orientation ϕ_Z (e) as a function of current velocity U.

scenario (Martinez et al., 2023b,a). Local drag and lift coefficients dependent on mesh are $C_D = 0.091$ and $C_L = -0.059$, respectively, and are used to generate results shown in Fig. 20(b).

Once the local drag and lift forces are calibrated, the simulations with current can be performed. In this case, significant wave height ($H_S = 1$ m) and peak period ($T_P = 10$ s) remain constant and the effect of current velocity and ballast mass (Table 6) are explored. Fig. 21 shows how the descent process is influenced by the current and how it differs from Fig. 6. At point (2), the anchor will reach a lower equilibrium depth as it gets lifted and pushed backwards by the current, instead of hanging under the vessel stern. At point (3) the anchor will be highly influenced by the current, where it will see a significant drift in the current direction.

In order to quantify how underwater currents influence the positioning stage of the anchor, let us consider their effect on the anchor's position (Z, Y and X) and orientation (Φ_Z, Φ_Y, and Φ_X) prior to releasing the winch. It is expected that both vertical (Z) and lateral (Y) displacements will decrease and increase, respectively with the current velocity U. To address that, we can increase amount of ballast pumped into the anchor, which should allow the lift forces responsible for such a behaviour to be overcome. This is illustrated in Fig. 22(a) & (c), which confirms that if the anchor's weight is high enough, the lift force due to the current can be negated, ensuring an equilibrium position with lower lateral drift and higher depth below the stern can be achieved. As the anchor is lifted up by the current, it is also dragged in the direction of current (Fig. 22(c)), though this distance is limited by the slack on the cable. The X position of the anchor (Fig. 22(e)) is not

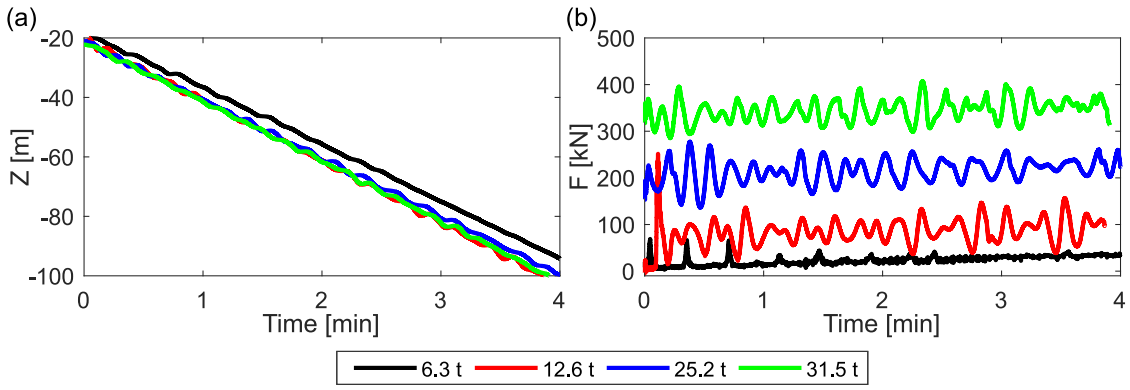

Fig. 24. Time histories of the anchor's vertical position (a) and winch force (b) for anchors with different ballast masses.

influenced by presence of current as the vessel is positioned parallel to it, but as explained in Section 4.3.1, the initial orientation of the anchor (yaw) will induce counter intuitive drift in X direction as the anchor retains 6 degrees-of-freedom. Note that the X and Y data shown in panels (c) and (e) is normalised to the initial (resting) position, hence both figures start at 0. The anchor's orientation is not influenced by its overall weight but currents can induce an increase in yaw (Fig. 22(b)) and pitch (Fig. 22(d), but not in roll (Fig. 22(f)).

As a next step, let us consider what happens with the anchor from the point the winch is released. This is studied in detail through the 3D descent trajectories obtained for winch velocity of $V_W = 0.35$ m/s and current flow velocities U between 0 and 1 kn. By repeating the analysis for selected cases of ballast mass ($m_B = 6.3$ t, $m_B = 12.6$ t, $m_B = 25.2$ t, $m_B = 31.5$ t) it is possible to verify how one can counteract the influence of strong currents on the anchor's trajectory as it descends to the seabed. This is illustrated in Fig. 23, where panels (a)–(d) correspond to the ballast masses listed above. Note, that the specific values of the ballast mass considered here, are multiples of ballast mass used in the base case (See Section 4.3.2) and were chosen to observe a general influence of ballast mass on the anchor's trajectory. The X and Y data is normalised with respect to its initial position. At lower flows and highest ballast cases (Fig. 23(d)), the anchor lands almost exactly at its initial position on X-Y plane. However, for higher current velocity and for the lightest ballast case (Fig. 23(a)), the anchor lands almost 180 m away from the initial position in the direction of the flow Y. This is related to the low effective weight of the anchor in water, as the underwater currents are able to induce its extreme drift on the way to the seabed. In the cross-flow direction X, the furthest the anchor lands is around 8 m from its initial position. It is clear that the drift of the anchor decreases as the amount of ballast increases and increases with the current velocity. In order to expand the operational weather conditions during future offshore installations of the variable buoyancy anchors, it will be therefore beneficial to increase the initial amount of ballast pumped into an anchor, so that high drift can be avoided if strong underwater currents are present in the particular location. Increasing ballast mass has also a stabilising effect in terms of yaw induced on the anchor, ϕ_Z, as shown in panel (e) of Fig. 23. Overall, the yaw angle stabilises as the current velocity increases and decreases with amount of ballast pumped into the anchor. This is an important observation, that will limit any winch cable entanglement issues during future offshore deployment.

Finally, we consider the effect of an increased ballast mass on the descent time and the winch forces observed. Since the simulations described in this section are run with a fixed winch velocity, there should not be any significant change in descent time. Likewise, the winch force is expected to change only by accounting for increased ballast mass. This is demonstrated through time histories of the vertical position (a) and winch force amplitude (b) for different ballast masses, shown in Fig. 24. Note, that the cases presented here are for $U = 0$ kn so that effect of ballast mass can be studied alone. It appears that in all instances, it takes the same amount of time (4 min) for the anchor to descend, but this is related to a fixed winch velocity. So the increase in ballast mass does not translate into an increase in anchor's descent velocity. However, looking at the winch force time series, we clearly observe that the tension in the cable increases with weight and the wave-induced oscillations (see Section 4.3.1) are more visible. These vibrations have the same amplitude for all ballast masses, except for the lightest case, which is the base case from Section 4.3.1. In practice this means that there is a weight-specific ideal winch velocity at which $V_A = V_W$ (Fig. 15), that will need to be identified when planning future offshore installation of such anchors in areas of high underwater currents.

5. Conclusions

Virtual prototyping of the deployment of a novel variable buoyancy anchor design using a real-physics Marine Simulator is described in this work. The anchor has a variable, controllable buoyancy, which means that it can float and be towed from harbour to the deployment location. Consequently, the installation can be done utilising just a winch instead of a heavy-lift crane, that requires a larger, higher emission, and more expensive vessel. The purpose of the detailed analysis presented here was to aid and de-risk the future offshore deployment of variable buoyancy anchors, such as that developed by Aubin Group and Oceneatics, thereby accelerating its Technology Readiness Level (TRL) and providing suitable alternative for traditional gravity based anchors. Moreover, such analysis allows better preparation and planning of future field trials of this technology, by identifying and verifying the importance of certain operating parameters for the proposed deployment scenario of variable buoyancy anchors. This in turn will provide novel and sustainable solution for existing and future floating wind projects (e.g. Celtic sea, ScotWind, Innovation and Targeted Oil and Gas (INTOG) Decarbonisation).

A number of operational and environmental parameters have been considered during the virtual prototyping of the variable buoyancy anchor system presented in this paper. This included detailed analysis of winch velocity, ballast pump rate, ballast mass, underwater current velocity, significant wave height and their effect on the overall installation process (e.g. positioning, descent stages, anchor's drift due to environmental loading, winch force and coupling between vessel's heave and anchor's vertical position). For example, winch velocity is an important parameter for the deployment process, as at slower rates it can negatively impact the forces acting on the winch and transmit the vessel's heave motions to the anchor as it descends through the water column. On the other hand, the winch cable guides the anchor during its descent, so increasing the velocity too much results in anchor's drift.

There is a clear trade-off here, as using slower winch velocities results in a longer descent time and increased amplitude of oscillations related to vessel's heave, while at the same time providing lower deviations in horizontal directions. Moreover, it is possible to identify an optimal winch velocity, that will be close to anchor's free fall velocity in water, as it reduces winch force amplitude during descent and ensures optimal conditions regarding anchor's orientation (yaw), thereby reducing the risk of entanglement of the winch cable and hoses. The winch force variation can be further optimised during installation phase by utilising passive heave compensation devices available within offshore industry. Increased drift of the anchor in the direction of waves for higher winch velocities can be addressed by either adjusting the vessel's position just before the anchor touches the seabed or by carefully estimating the appropriate initial position of the vessel based on site weather conditions and results presented here.

Ballast pump rate has a direct influence on the time it takes for the variable buoyancy anchor to take its position under stern of the vessel (before its descent to the seabed), so it is beneficial to keep it high to limit the exposure of the anchor to wave loading. On the other hand the main factor, that can significantly disrupt the deployment of variable buoyancy anchors due to their low weight in water, is the underwater current resulting in significant drift of the anchor. This decreases as the amount of ballast increases and increases with the current velocity. In order to expand the operational weather conditions during future offshore installations, it will be beneficial therefore to increase the initial amount of ballast pumped into an anchor, so that high drift can be avoided at strong underwater currents locations. In such conditions, one will need to determine the anchor's free fall velocity, so that optimal winch velocity can be applied ($V_W \approx V_A$). Increasing ballast mass has also a stabilising effect in terms of the yaw induced on the anchor. Overall, the yaw angle reaches a threshold as the current velocity increases and decreases with the amount of ballast pumped into the anchor. This is an important observation, that will limit any winch cable entanglement issues in future offshore applications.

Finally, the effect of waves, particularly significant wave height, on the simulated deployment of variable buoyancy anchors has been considered in detail. Compared to ballast pump rate, underwater current and winch velocity, the significant wave height of the JONSWAP spectrum considered, has a limited influence of the feasibility of deploying variable buoyancy anchors. Increasing significant wave height will increase the amplitude of the anchor's oscillations in the X-Y plane, particularly closer to surface where the anchor gets "caught" in the wave orbitals that reach further down the water column. These vibrations diminish as the anchor is deeper in the water column. Nevertheless, vibrations observed on the way to the seabed have little impact on the overall landing position of the anchor itself, though one can see a weak correlation between wave height and increased drift in the wave direction. The overall effect of significant wave height on the variable anchor's orientation is minimal, and the main parameter that can induce yaw, possibly leading to cable entanglement issues, is the winch velocity that from the point of future offshore deployment needs special attention.

This work has demonstrated that virtual prototyping can be a useful tool to expand our understanding of the offshore deployment of technologies currently under development, such as variable buoyancy anchors. Through the analysis presented here, it was possible to identify importance and significance of number of operational parameters, that will need to be considered when planning in detail future field trials. Additionally, the feasibility of deploying variable buoyancy anchors has been demonstrated in a wide range of possible weather conditions, that will contribute to de-risking future offshore installation. The developed model can be further utilised and improved once a specific location for deployment of this novel type of anchors is chosen. This will contribute to eliminating any uncertainties in terms of system parameters or environmental conditions, that may have influenced studies presented in this paper. Additionally, the research methods used in this study allow for performing simulations in real time, which demonstrates a significant computational advantage over other modelling software that could be potentially used for such a study (e.g. OrcaFlex, OpenFAST). In terms of future work in this topic, the model presented here will be used to explore towing dynamics of variable buoyancy anchors. Moreover, the Marine Simulator used in this study will be utilised for analysing other new technologies, such as for example novel concepts of floating wind turbines and mooring lines load reduction techniques.

CRediT authorship contribution statement

Rodrigo Martinez: Writing – original draft, Formal analysis, Investigation, Visualization. **Sergi Arnau:** Data curation, Investigation. **Callum Scullion:** Conceptualisation, Validation. **Paddy Collins:** Conceptualisation, Validation. **Richard D. Neilson:** Funding acquisition, Writing – review & editing. **Marcin Kapitaniak:** Funding acquisition, Writing – review & editing, Supervision, Visualization, Project administration.

Declaration of competing interest

The authors declare that they have no known competing financial interests or personal relationships that could have appeared to influence the work reported in this paper.

Data availability

Data will be made available on request.

Acknowledgements

The research presented in this paper has been primarily sponsored by EPSRC's Supergen ORE Hub & ORE Catapult Floating Offshore Wind Centre of Excellence (grant number FF2021-1040). The authors acknowledge funding received from Energy Technology Partnership Knowledge Exchange Network scheme (grant number PR057-ME) that provided additional funding to support this work. The authors wish to thank Oceanetics Inc. and Aubin Group for their support towards this project. This work has benefited from the support and funding received from Net Zero Technology Centre and The University of Aberdeen through their partnership in The National Decommissioning Centre (NDC) and The Scottish Government's Decommissioning Challenge Fund in part-funding the establishment of the Marine Simulator research facility at the NDC.

Appendix. Test matrices

See Tables 1–6.

Table 1
Buoyancy parameters.

Case	Q [m^3/min]	Case	Q [m^3/min]
1	0.04	11	1.07
2	0.09	12	1.07
3	0.17	13	1.24
4	0.26	14	1.33
5	0.34	15	1.37
6	0.47	16	1.37
7	0.60	17	1.45
8	0.73	18	1.62
9	0.85	19	1.87
10	1.02		

Table 2
Positioning parameters.

H_S [m]; T_P [s] \ V_W [m/s]	0.05	0.09	0.13	0.18	0.21	0.25	0.29	0.34	0.42	0.46	0.50	0.55
1.0, 10	✓	✓	✓	✓	✓	✓	✓	✓	✓	✓	✓	✓
1.5, 10	✓	✓	✓	✓	✓	✓	✓	✓	✓	✓	✓	✓
2.0, 10	✓	✓	✓	✓	✓	✓	✓	✓	✓	✓	✓	✓
2.5, 10	✓	✓	✓	✓	✓	✓	✓	✓	✓	✓	✓	✓
3.0, 10	✓	✓	✓	✓	✓	✓	✓	✓	✓	✓	✓	✓
3.5, 10	✓	✓	✓	✓	✓	✓	✓	✓	✓	✓	✓	✓
4.0, 10	✓	✓	✓	✓	✓	✓	✓	✓	✓	✓	✓	✓
5.0, 10	✓	✓	✓	✓	✓	✓	✓	✓	✓	✓	✓	✓

Table 3
Positioning parameters – Continued.

H_S [m]; T_P [s] \ V_W [m/s]	0.62	0.67	0.72	0.73	0.75	0.80	0.85	0.90	0.93	0.97	1.03
1.0, 10	✓	✓	✓	✓	✓	✓	✓	✓	✓	✓	✓
1.5, 10	✓	✓	✓	✓	✓	✓	✓	✓	✓	✓	✓
2.0, 10	✓	✓	✓	✓	✓	✓	✓	✓	✓	✓	✓
2.5, 10	✓	✓	✓	✓	✓	✓	✓	✓	✓	✓	✓
3.0, 10	✓	✓	✓	✓	✓	✓	✓	✓	✓	✓	✓
3.5, 10	✓	✓	✓	✓	✓	✓	✓	✓	✓	✓	✓
4.0, 10	✓	✓	✓	✓	✓	✓	✓	✓	✓	✓	✓
5.0, 10	✓	✓	✓	✓	✓	✓	✓	✓	✓	✓	✓

Table 4
Descent parameters – Base case.

V_W [m/s]	H_S [m]	T [s]
0.025	1	10
0.040	1	10
0.050	1	10
0.060	1	10
0.075	1	10
0.090	1	10
0.100	1	10
0.125	1	10
0.150	1	10
0.160	1	10
0.170	1	10
0.175	1	10
0.180	1	10
0.190	1	10
0.200	1	10
0.210	1	10
0.220	1	10
0.225	1	10
0.250	1	10
0.260	1	10

V_A [m/s]	H_S [m]	T [s]
0.270	1	10
0.275	1	10
0.290	1	10
0.300	1	10
0.300	1	10
0.310	1	10
0.320	1	10
0.325	1	10
0.330	1	10
0.340	1	10
0.350	1	10
0.350	1	10
0.360	1	10
0.375	1	10
0.380	1	10
0.400	1	10
0.425	1	10
0.450	1	10
0.475	1	10
0.500	1	10

Table 5
Descent parameters – Waves.

H_S [m]; T_P [s] \ V_W [m/s]	0.30	0.32	0.34	0.36	0.38	0.40	0.42	0.44	0.46	0.48	0.50
2.0, 10	✓	✓	✓	✓	✓	✓	✓	✓	✓	✓	✓
2.5, 10	✓	✓	✓	✓	✓	✓	✓	✓	✓	✓	✓
3.0, 10	✓	✓	✓	✓	✓	✓	✓	✓	✓	✓	✓
3.5, 10	✓	✓	✓	✓	✓	✓	✓	✓	✓	✓	✓
4.0, 10	✓	✓	✓	✓	✓	✓	✓	✓	✓	✓	✓
5.0, 10	✓	✓	✓	✓	✓	✓	✓	✓	✓	✓	✓

Table 6
Descent parameters – Currents.

m_B [t]; \ U [kn]	0.00	0.09	0.18	0.27	0.38	0.49	0.58	0.69	0.76	0.83	0.90	1.01
6.3	✓	✓	✓	✓	✓	✓	✓	✓	✓	✓	✓	✓
12.6	✓	✓	✓	✓	✓	✓	✓	✓	✓	✓	✓	✓
25.2	✓	✓	✓	✓	✓	✓	✓	✓		✓	✓	✓
31.5	✓	✓	✓	✓	✓	✓	✓	✓		✓	✓	✓

References

Algoryx Simulation AB, 2019. AGX dynamics. Aug. 2022, [Online]. Available: https://www.algoryx.se/agx-dynamics/.

Bjerkseter, C., Agotnes, A., 2013. Levelised costs of energy for offshore floating wind turbine concepts. (Master's thesis). Norwegian University of Life Sciences, Department of Mathematical Sciences and Technology.

Boukhanovsky, A.V., Lopatoukhin, L.J., Guedes Soares, C., 2007. Spectral wave climate of the North Sea. Appl. Ocean Res. 29 (3), 146–154. http://dx.doi.org/10.1016/j.apor.2007.08.004, URL https://www.sciencedirect.com/science/article/pii/S0141118707000545.

Brown, D.T., 2005. Mooring systems. In: Handbook of Offshore Engineering. Elsevier, pp. 663–708. http://dx.doi.org/10.1016/B978-0-08-044381-2.50015-1, URL https://linkinghub.elsevier.com/retrieve/pii/B9780080443812500151.

Bye, R.T., Osen, O.L., Pedersen, B.S., 2015. A Computer-Automated Design Tool For Intelligent Virtual Prototyping of Offshore Cranes. ECMS, pp. 147–156. http://dx.doi.org/10.7148/2015-0147, URL http://www.scs-europe.net/dlib/2015/2015-0147.htm.

Cheng, X., Li, G., Skulstad, R., Chen, S., Hildre, H.P., Zhang, H., 2019a. Modeling and analysis of motion data from dynamically positioned vessels for sea state estimation. In: 2019 International Conference on Robotics and Automation (ICRA). IEEE, pp. 6644–6650. http://dx.doi.org/10.1109/ICRA.2019.8794069, URL https://ieeexplore.ieee.org/document/8794069/.

Cheng, X., Li, G., Skulstad, R., Major, P., Chen, S., Hildre, H.P., Zhang, H., 2019b. Data-driven uncertainty and sensitivity analysis for ship motion modeling in offshore operations. Ocean Eng. 179, 261–272. http://dx.doi.org/10.1016/j.oceaneng.2019.03.014.

Chu, Y., Hatledal, L.I., Æsøy, V., Ehlers, S., Zhang, H., 2018. An object-oriented modeling approach to virtual prototyping of marine operation systems based on functional mock-up interface co-simulation. J. Offshore Mech. Arct. Eng. 140, http://dx.doi.org/10.1115/1.4038346, URL https://asmedigitalcollection.asme.org/offshoremechanics/article/doi/10.1115/1.4038346/395243/An-ObjectOriented-Modeling-Approach-to-Virtual.

Davies, A.M., Furnes, G.K., 1980. Observed and computed M2 tidal currents in the North Sea. J. Phys. Oceanogr. 10, 237–257, URL https://journals.ametsoc.org/view/journals/phoc/10/2/1520-0485_1980_010_0237_oacmtc_2_0_co_2.xml.

Davies, A., Hastings, A., 2023. Greenhouse gas emissions from decommissioning manmade structures in the marine environment; current trends and implications for the future. J. Mar. Sci. Eng. 11 (6), URL https://www.mdpi.com/2077-1312/11/6/1133.

Dean, R.G., Dalrymple, R.A., 1984. Water Wave Mechanics for Engineers and Scientists. Prentice-Hall, Englewood Cliffs.

Det Norske Veritas, 2011. Recommended practice DNV-RP-H103 - modelling and analysis of marine operations. Technical Report, URL http://www.dnv.com.

Det Norske Veritas, 2014. Recommended practice DNV-RP-C205 - environmental conditions and environmental loads. Technical Report, URL www.dnvgl.com.

Det Norske Veritas, 2016. Standard - DNVGL-ST-0126 - support structures for wind turbines. Technical Report, URL http://www.dnvgl.com.

Det Norske Veritas, 2018. Standard - DNVGL-ST-0119 - floating wind turbine structures. Technical Report, URL http://www.dnvgl.com.

Harvey, M., Strivens, S., Evans, H., Morris, A., 2022. Floating wind joint industry project - phase IV summary report. Technical Report, The Carbon Trust.

Hasselmann, K., Barnett, T., Bouws, E., Carlson, H., Cartwright, D., Enke, K., Ewing, J., Gienapp, H., Hasselmann, D., Kruseman, P., Meerburg, A., Mller, P., Olbers, D., Richter, K., Sell, W., Walden, H., 1973. Measurements of wind-wave growth and swell decay during the Joint North Sea Wave Project (JONSWAP). In: Ergnzungsheft Zur Deutschen Hydrographischen Zeitschrift Reihe. p. 95, A(8) (Nr. 12).

Hedges, T.S., 1987. Combinations of waves and currents: An introduction. Proc. Inst. Civ. Eng. 82 (3), 567–585. http://dx.doi.org/10.1680/iicep.1987.319.

Henry, D., 2019. Stokes drift in equatorial water waves, and wave–current interactions. Deep Sea Res. II 160, 41–47, URL https://www.sciencedirect.com/science/article/pii/S0967064518301334.

Håvold, J.I., Nistad, S., Skiri, A., Ødegård, A., 2015. The human factor and simulator training for offshore anchor handling operators. Saf. Sci. 75, 136–145. http://dx.doi.org/10.1016/j.ssci.2015.02.001, URL https://linkinghub.elsevier.com/retrieve/pii/S092575351500020X.

Ikhennicheu, M., Lynch, M., Doole, S., Borisade, F., Matha, D., Dominguez, J.L., Vicente, R.D., Habekost, T., Ramirez, L., Potestio, S., Molins, C., Trubat, P., 2020. D2.1 - review of the state of the art of mooring and anchoring designs, technical challenges and identification of relevant DLCs. Technical Report, COREWIND.

James, R., Ros, M.C., 2015. Floating offshore wind: Market and technology review. Technical Report, The Carbon Trust.

James, R., Weng, W.-Y., Spradbery, C., Jones, J., Matha, D., Mitzlaff, A., Ahilan, R.V., Frampton, M., Lopes, M., 2018. Floating wind joint industry project - phase I summary report. Technical Report, The Carbon Trust.

Li, G., Homlong, E., Zhang, H., Dimmen, B.A., 2017. Integration of Visual Focus into Marine Operation Simulator for Behavior Observation and Analysis. IEEE, pp. 1–7. http://dx.doi.org/10.1109/OCEANSE.2017.8084601, URL http://ieeexplore.ieee.org/document/8084601/.

Liu, Y., Li, S., Yi, Q., Chen, D., 2016. Developments in semi-submersible floating foundations supporting wind turbines: A comprehensive review. Renew. Sustain. Energy Rev. 60, 433–449. http://dx.doi.org/10.1016/j.rser.2016.01.109, URL https://linkinghub.elsevier.com/retrieve/pii/S1364032116001398.

Ma, K.-T., Luo, Y., Kwan, T., Wu, Y., 2019. Mooring for floating wind turbines. In: Mooring System Engineering for Offshore Structures. Elsevier, pp. 299–315. http://dx.doi.org/10.1016/B978-0-12-818551-3.00015-6, URL https://linkinghub.elsevier.com/retrieve/pii/B9780128185513000156.

Major, P., Zhang, H., Hildre, H.P., Edet, M., 2021. Virtual prototyping of offshore operations: a review. Ship Technol. Res. 68, 84–101. http://dx.doi.org/10.1080/09377255.2020.1831840, URL https://www.tandfonline.com/doi/full/10.1080/09377255.2020.1831840.

Martinez, R., Arnau, S., Scullion, C., Collins, P., Neilson, R.D., Kapitaniak, M., 2023a. Deployment feasibility studies of variable buoyancy anchors for floating wind applications. In: Dimitrovová, Z., Biswas, P., Gonçalves, R., Silva, T. (Eds.), Recent Trends in Wave Mechanics and Vibrations. Springer International Publishing, Cham, pp. 447–456, URL https://link.springer.com/chapter/10.1007/978-3-031-15758-5_45.

Martinez, R., Arnau, S., Scullion, C., Collins, P., Neilson, R.D., Kapitaniak, M., 2023b. Virtual prototyping of a floating wind farm anchor during underwater towing operations. In: Dimitrovová, Z., Biswas, P., Gonçalves, R., Silva, T. (Eds.), Recent Trends in Wave Mechanics and Vibrations. Springer International Publishing, Cham, pp. 555–564, URL https://link.springer.com/chapter/10.1007/978-3-031-15758-5_57.

MET Office, 2010. Fact sheet 6 — The Beaufort scale. Technical Report, The National Meteorological Library and Archive.

Micallef, D., Rezaeiha, A., 2021. Floating offshore wind turbine aerodynamics: Trends and future challenges. Renew. Sustain. Energy Rev. 152, 111696. http://dx.doi.org/10.1016/j.rser.2021.111696, URL https://linkinghub.elsevier.com/retrieve/pii/S1364032121009709.

Myhr, A., Bjerkseter, C., Ågotnes, A., Nygaard, T.A., 2014. Levelised cost of energy for offshore floating wind turbines in a life cycle perspective. Renew. Energy 66, 714–728. http://dx.doi.org/10.1016/j.renene.2014.01.017, URL https://linkinghub.elsevier.com/retrieve/pii/S0960148114000469.

O'Connor, M., Lewis, T., Dalton, G., 2013. Weather window analysis of Irish west coast wave data with relevance to operations & maintenance of marine renewables. Renew. Energy 52, 57–66, URL https://www.sciencedirect.com/science/article/pii/S0960148112006660.

Offshore Simulator Center AS, 2020. Aug. 2022, [Online]. Available: https://osc.no/.

ORE Catapult, 2021. Decarbonising maritime operations in North Sea offshore wind O&M: Innovation roadmap produced for the UK government DfT and FCDO. URL https://www.gov.uk/government/publications/decarbonising-offshore-wind-operations-and-maintenance-roadmap.

Peregrine, D., 1976. Interaction of water waves and currents. In: Yih, C.-S. (Ed.), In: Advances in Applied Mechanics, vol. 16, Elsevier, pp. 9–117. http://dx.doi.org/10.1016/S0065-2156(08)70087-5, URL http://www.sciencedirect.com/science/article/pii/S0065215608700875.

Pierson Jr., W.J., Moskowitz, L., 1964. A proposed spectral form for fully developed wind seas based on the similarity theory of S.A. Kitaigorodskii. J. Geophys. Res. (1896-1977) 69 (24), 5181–5190, URL https://agupubs.onlinelibrary.wiley.com/doi/abs/10.1029/JZ069i024p05181.

Pillai, A., Gordelier, T., Thies, P., Dormenval, C., Wray, B., Parkinson, R., Johanning, L., 2022. Anchor loads for shallow water mooring of a 15 MW floating wind turbine — Part I: Chain catenary moorings for single and shared anchor scenarios. Ocean Eng. 266, 111816, URL https://www.sciencedirect.com/science/article/pii/S0029801822011611.

Pratt, M.J., 1995. Virtual prototypes and product models in mechanical engineering. In: Rix, J., Haas, S., Teixeira, J. (Eds.), Virtual Prototyping: Virtual Environments and the Product Design Process. Springer US, Boston, MA, pp. 113–128. http://dx.doi.org/10.1007/978-0-387-34904-6_10.

Sandberg, S.Å., 2014. Interactive simulation of hydrodynamics for arbitrarily shaped objects. (Master's thesis). Umeå University, Faculty of Science and Technology, Umeå, Sweden.

Sanfilippo, F., 2016. A multi-sensor system for enhancing situational awareness in offshore training. In: 2016 International Conference on Cyber Situational Awareness, Data Analytics and Assessment, CyberSA 2016. Institute of Electrical and Electronics Engineers Inc., http://dx.doi.org/10.1109/CyberSA.2016.7503280.

Sanfilippo, F., 2017. A multi-sensor fusion framework for improving situational awareness in demanding maritime training. Reliab. Eng. Syst. Saf. 161, 12–24. http://dx.doi.org/10.1016/j.ress.2016.12.015.

Sanfilippo, F., Hatledal, L.I., Styve, A., Pettersen, K.Y., Zhang, H., 2016. Integrated flexible maritime crane architecture for the offshore simulation centre AS (OSC): A flexible framework for alternative maritime crane control algorithms. IEEE J. Ocean. Eng. 41, 450–461. http://dx.doi.org/10.1109/JOE.2015.2439891.

Sellar, B., Wakelam, G., 2018. Characterisation of tidal flows at the European Marine Energy Centre in the absence of ocean waves. Energies 11 (1), 176.

Spearman, D.K., Strivens, S., Matha, D., Cosack, N., Macleay, A., Regelink, J., Patel, D., Walsh, T., 2020. Floating wind joint industry project - phase II summary report. Technical Report, The Carbon Trust.

Stevens, R.F., Rahim, A., 2014. Mooring anchors for marine renewable energy foundations.

Stewart, G., Muskulus, M., 2016a. A review and comparison of floating offshore wind turbine model experiments. Energy Procedia 94, 227–231, 13th Deep Sea Offshore Wind R&D Conference, EERA DeepWind 2016.

Stewart, G., Muskulus, M., 2016b. A review and comparison of floating offshore wind turbine model experiments. Energy Procedia 94, 227–231. http://dx.doi.org/10.1016/j.egypro.2016.09.228, URL https://linkinghub.elsevier.com/retrieve/pii/S1876610216309146.

Stokes, A., 2014. Decommissioning costs can be reduced. OTC-25247-MS, Offshore Technology Conference, Houston, USA.

Strivens, S., Northridge, E., Evans, H., Harvey, M., Camp, T., Terry, N., 2021. Floating wind joint industry project - phase III summary report. Technical Report, The Carbon Trust.

Sutherland, D.R.J., Sellar, B.G., Harding, S., Bryden, I., 2013. Initial flow characterisation utilising turbine and seabed installed acoustic sensor arrays. In: Proceedings of the 10th European Wave and Tidal Energy Conference. Aalborg, pp. 1–8.

Vindenes, H., Orvik, K.A., Søiland, H., Wehde, H., 2018. Analysis of tidal currents in the north sea from shipboard acoustic Doppler current profiler data. Cont. Shelf Res. 162, 1–12.

Walker, R.T., Nieuwkoop-Mccall, J.V., Johanning, L., Parkinson, R.J., 2013. Calculating weather windows: Application to transit, installation and the implications on deployment success. Ocean Eng. 68, 88–101.

Wang, G.G., 2003. Definition and review of virtual prototyping. J. Comput. Inf. Sci. Eng. 2 (3), 232–236. http://dx.doi.org/10.1115/1.1526508.

Webb, A., Fox-Kemper, B., 2015. Impacts of wave spreading and multidirectional waves on estimating Stokes drift. Ocean Model. 96, 49–64, URL https://www.sciencedirect.com/science/article/pii/S1463500314001942.

Weber, J.E.H., 2021. On the Stokes drift in traveling surface pulses. Ocean Model. 166, 101847, URL https://www.sciencedirect.com/science/article/pii/S1463500321000998.

WindEurope, 2022. Wind energy in Europe - 2021 Statistics and the outlook for 2022–2026. Technical Report, WindEurope.

Xu, J., Ataei, B., Halse, K.H., Hildre, H.P., Mikalsen, E.T., 2020. Virtual prototyping of a low-height lifting system for offshore wind turbine installation. In: Volume 9: Ocean Renewable Energy. American Society of Mechanical Engineers, http://dx.doi.org/10.1115/OMAE2020-19166, URL https://asmedigitalcollection.asme.org/OMAE/proceedings/OMAE2020/84416/Virtual,%20Online/1093186.

Yuan, S., Major, P., Zhang, H., 2020. Flexible riser replacement operation based on advanced virtual prototyping. Ocean Eng. 210, http://dx.doi.org/10.1016/j.oceaneng.2020.107502.